The Astrophysical Journal, 979:85 (19pp), 2025 January 20 https://doi.org/10.3847/1538-4357/ad9b0d

Dependence of Metal Enrichment of Nuclear Star Clusters on Galaxy Stellar Mass

Wenhe Lyu[1,2], Hong-Xin Zhang[1,2], Sanjaya Paudel[3,4], Tie Li[1,2], Yimeng Tang[5], Guangwen Chen[6], Xu Kong[1,7,8], and Eric W. Peng[9]

[1] School of Astronomy and Space Sciences, University of Science and Technology of China, Hefei, 230026, People's Republic of China; hzhang18@ustc.edu.cn
[2] CAS Key Laboratory for Research in Galaxies and Cosmology, Department of Astronomy, University of Science and Technology of China, Hefei 230026, People's Republic of China
[3] Department of Astronomy, Yonsei University, Seoul, 03722, Republic of Korea
[4] Center for Galaxy Evolution Research, Yonsei University, Seoul, 03722, Republic of Korea
[5] Department of Astronomy and Astrophysics, University of California Santa Cruz, 1156 High Street, Santa Cruz, CA 95064, USA
[6] Sub-department of Astrophysics, University of Oxford, Keble Road, Oxford, OX1 3RH, UK
[7] Deep Space Exploration Laboratory/Department of Astronomy, University of Science and Technology of China, Hefei, 230026, People's Republic of China
[8] Frontiers Science Center for Planetary Exploration and Emerging Technologies, University of Science and Technology of China, Hefei, Anhui, 230026, People's Republic of China
[9] NSF's NOIRLab, 950 N. Cherry Avenue, Tucson, AZ 85719, USA

Received 2024 September 6; revised 2024 November 27; accepted 2024 December 3; published 2025 January 20

Abstract

Nuclear star clusters (NSCs) are commonly found in the centers of galaxies, but their dominant formation mechanisms remain elusive. We perform a consistent analysis of stellar populations of 97 nearby NSCs, based on spectroscopic data from the Very Large Telescope. The sample covers a galaxy stellar mass range of 10^7–10^{11} $M_\odot$ and is more than 3 times larger than any previous study. We identify three galaxy stellar mass regimes with distinct NSC properties. In the low-mass regime of $\log M_{\rm host} \lesssim 8.5$ ($M_{\rm host}$ is in units of $M_\odot$), nearly all NSCs have metallicities lower than their circum-NSC host but similar to those of typical red globular clusters (GCs), supporting the GC inspiral–merger scenario of NSC formation. In the high-mass regime of $\log M_{\rm host} \gtrsim 9.5$, nearly all NSCs have higher metallicities than their circum-NSC host and red GCs, suggesting significant contributions from in situ star formation. In the intermediate-mass regime, a comparable fraction of NSCs have higher or lower metallicities than their circum-NSC host and red GCs, with no clear dependence on NSC mass, suggesting intermittent in situ star formation. The majority of NSCs with higher metallicities than their host exhibit a negative age–metallicity correlation, providing clear evidence of long-term chemical enrichment. The average metallicity difference between NSC and host peaks broadly around $\log M_{\rm host} \sim 9.8$ and declines toward both higher and lower galaxy masses. We find that the efficiency of dynamical-friction-driven inspiral of GCs observed in present-day galaxies can explain the NSC mass at $\log M_{\rm host} \lesssim 9.5$ but falls short of observed ones at higher galaxy mass, reinforcing our conclusions based on stellar population analysis.

Unified Astronomy Thesaurus concepts: Galaxy nuclei (609); Metallicity (1031); Stellar populations (1622); Galaxy structure (622); Star clusters (1567); Globular star clusters (656)

1. Introduction

Nuclear star clusters (NSCs) are dense and massive star clusters located near the centers of galaxies. The size and mass of NSCs span a range that partially overlaps with that of globular clusters (GCs) at the low end, and reaches up to several tens of parsecs in half-light radius R_e and several hundred million solar masses at the high end (e.g., P. Côté et al. 2006; I. Y. Georgiev et al. 2016; R. Sánchez-Janssen et al. 2019; N. Neumayer et al. 2020). The highest stellar densities in the Universe are found in NSCs. NSCs may serve as favorable formation sites of the elusive intermediate-mass black holes (IMBHs; e.g., M. C. Miller & V. M. Lauburg 2009; G. Fragione & J. Silk 2020; D. Atallah et al. 2023). Moreover, tidally stripped NSCs are considered to be an important contributor to the still mysterious ultracompact dwarf galaxies (e.g., H.-X. Zhang et al. 2015, 2018; C. Liu et al. 2015, 2020; C. P. Ahn et al. 2017; R. J. Mayes et al. 2021; G. Chen et al. 2022; K. Wang et al. 2023).

The formation mechanism of NSCs and its connection with host galaxies are not well understood. Statistical studies of the fraction of galaxies that host NSCs (i.e., the nucleation fraction) in various environments (e.g., P. Côté et al. 2006; M. L. Turner et al. 2012; M. den Brok et al. 2014; R. Sánchez-Janssen et al. 2019; N. Hoyer et al. 2021) suggest that the nucleation fraction has a strong dependence on galaxy stellar mass and reaches a maximum of ∼90% in galaxies with $M_\star \sim 10^9$–$10^{9.5}$ $M_\odot$ and drops steadily toward both lower and higher masses.

The mass of NSCs correlates positively with the stellar mass of the host galaxies, albeit with a substantial scatter. The correlation appears to be sublinear, suggesting that lower-mass galaxies tend to have a higher fraction of mass in NSCs than do higher-mass galaxies (e.g., R. Sánchez-Janssen et al. 2019; N. Neumayer et al. 2020; N. Hoyer et al. 2023b). There is extensive evidence that NSCs may coexist with central (super) massive black holes in many galaxies with stellar masses above 10^9 $M_\odot$ (see N. Neumayer & C. J. Walcher 2012; N. Neumayer et al. 2020, and references therein). The drop in nucleation fraction toward the higher-mass end may be attributed to the influence of massive black holes (e.g., M. Arca-Sedda & R. Capuzzo-Dolcetta 2014; F. Antonini et al. 2015).

The two commonly cited growth mechanisms for NSCs are GC inspiral and merger driven by dynamical friction (e.g., S. D. Tremaine et al. 1975; R. Capuzzo-Dolcetta 1993; J. M. Lotz et al. 2001; M. Arca-Sedda & R. Capuzzo-Dolcetta 2014) and in situ star formation triggered by torque-induced gas inflow (e.g., J. Silk et al. 1987; J. C. Mihos & L. Hernquist 1994; K. Bekki 2015; A. Feldmeier-Krause et al. 2015). The scenario of dynamical-friction-driven star cluster inspiral is expected to be an unavoidable physical process, and is usually used to explain the presence of metal-poor stellar populations found especially in the NSCs of dwarf galaxies (M. Alfaro-Cuello et al. 2020; K. Fahrion et al. 2020, 2021). Note that the surviving GC population can be quite different from the one that spirals into the galactic center. In the latter mechanism, NSCs are expected to have relatively extended star formation histories and to contain chemically enriched young stellar populations. The two distinct mechanisms are not necessarily mutually exclusive in reality. N. Guillard et al. (2016) propose a hybrid mechanism, whereby gas-bearing young massive star clusters spiral into the center of a galaxy due to dynamical friction and continue forming stars after migrating to the center.

Dynamical-friction-driven inspiral of massive GCs is probably unavoidable from a theoretical point of view, but observational verification is largely indirect (e.g., N. Neumayer et al. 2020). In particular, there appears to be a central deficit of massive GCs in many early-type galaxies (e.g., J. M. Lotz et al. 2001). The nucleation fraction seems to track the fraction of galaxies hosting GCs for low-mass early-type galaxies (R. Sánchez-Janssen et al. 2019). Recently, J. Román et al. (2023) found an unusually high concentration of GC candidates near the center of UGC 7346, and speculated that this may be an NSC caught in its early stage of formation through dynamical-friction-driven inspiral of GCs (see also R. Schiavi et al. 2021, for a similar discovery). On the other hand, the in situ formation scenario has a wealth of observational evidence (e.g., C. J. Walcher et al. 2006; A. C. Seth et al. 2006; N. Kacharov et al. 2018; K. Fahrion et al. 2021), with the NSC in our Milky Way being a notable example (e.g., A. Feldmeier-Krause et al. 2015).

Recent literature seems to reach a broad consensus that the dominant formation pathway has a strong connection with galaxy mass (P. Côté et al. 2006; M. Arca-Sedda & R. Capuzzo-Dolcetta 2014; N. Neumayer et al. 2020, and references therein), in the sense that NSCs grow primarily by dynamical-friction-driven GC infall and merger at a galaxy stellar mass much smaller than $10^9\ M_\odot$, while above the transition mass of $\sim 10^9\ M_\odot$, in situ star formation gradually becomes the dominant pathway. At the transition galaxy mass of $\sim 10^9\ M_\odot$ (the typical NSC mass being $\sim 10^6\ M_\odot$), both GC inspiral and in situ star formation play important roles. Such a formation pathway dependent on galaxy mass appears to be supported by several observational findings, such as NSC stellar populations dependent on galaxy mass (this work), NSC shapes (e.g., C. Spengler et al. 2017), and nucleation fractions. It is not clear, however, what drives this apparent mass-dependent dichotomy (N. Neumayer et al. 2020).

Stellar population properties provide important clues to the dominant formation pathways of NSCs. With the exception of the NSC in the Milky Way, where individual stars are well resolved, integrated-light spectroscopy is usually the practical choice for obtaining robust estimates of the stellar populations of extragalactic NSCs (e.g., J. Rossa et al. 2006; A. C. Seth et al. 2006; C. J. Walcher et al. 2006; S. Paudel et al. 2011; N. Kacharov et al. 2018; E. J. Johnston et al. 2020; K. Fahrion et al. 2021, 2022a). A general finding from these spectroscopic analyses is that NSCs in low-mass galaxies ($<10^9\ M_\odot$) tend to have light-weighted metallicities lower than their host galaxies, whereas NSCs in more massive galaxies tend to have higher stellar metallicities than their host galaxies. This is in line with the expectation of the dominant growth pathways mentioned above that are dependent on galaxy mass. However, the existing spectroscopic analysis of NSCs is limited to relatively small sample sizes, which makes it difficult to draw robust conclusions about the dependence of NSC stellar populations on host galaxy properties. So far, stellar population analyses of the largest samples of NSCs were performed by S. Paudel et al. (2011; 26 nucleated dwarf elliptical galaxies in the Virgo cluster) and K. Fahrion et al. (2021; 25 nucleated early-type galaxies mostly in the Fornax cluster).

Besides the relatively small sample size of previous spectroscopic analyses of stellar populations of NSCs, different studies usually differ in their adopted spectral extraction methods, stellar population models, or spectral modeling techniques. The potential systematic bias induced by these differences hinders a statistical analysis of literature samples based on a direct compilation of stellar population parameters derived from different studies. In this work, we collect high-quality archival optical spectra of nearby NSCs observed by various instruments on the Very Large Telescope (VLT), and perform a statistical analysis of the stellar population properties obtained through consistent spectral extraction and modeling.

The paper is structured as follows. A description of the sample and data reduction is given in Section 2 and the analysis method is given in Section 3. Results are presented in Section 4. The discussion and summary are given in Sections 5 and 6, respectively.

2. Sample and Data Reduction

2.1. Sample and Observations

Most of the spectroscopic observations of extragalactic NSCs have been carried out with VLT (also the Hubble Space Telescope; see, e.g., J. Rossa et al. 2006). We start with the catalog of nucleated galaxies in the Local Volume (I. D. Karachentsev et al. 2013), Virgo Cluster, and Fornax Cluster, as compiled by N. Hoyer et al. (2021), and search the ESO Science Archive for optical spectroscopic observations of the nuclear regions of these galaxies. The search returns 97 galaxies in total, among which 12 were observed with the X-Shooter spectrograph, 40 with the FORS2 spectrograph, and 45 with the MUSE spectrograph. We note that 29 of these NSCs do not have previous stellar population analyses based on spectral modeling. We download and calibrate the raw data of the 97 nucleated galaxies. A brief description of the sample and data observed by each instrument is given in Table 1.

2.1.1. X-Shooter Spectra

X-Shooter is a multiwavelength, medium-resolution long-slit spectrograph mounted at the UT3 Cassegrain focus of VLT (J. Vernet et al. 2011). It covers the entire ultraviolet to near-infrared wavelength range simultaneously with three spectroscopic arms: UVB (2980–5600 Å), VIS (5500–10200 Å), and NIR (10200–24800 Å).

Table 1
Detail of Nucleated Galaxies

(1) Name -	(2) R.A.(J2000) (deg)	(3) Decl.(J2000) (deg)	(4) $\log(M_{\rm host}/M_{\odot})$	(5) $\log(M_{\rm NSC}/M_{\odot})$	(6) Hubble Type -	(7) Instrument -	(8) Source -	(9) PID -
NGC 247	11.786	−20.760	9.258	6.25	6.9	X-Shooter	K18	084.B-0499
NGC 2784	138.081	−24.173	10.672	8.64[a]	−2.1	X-Shooter	Un	097.B-0435
NGC 300	13.723	−37.684	9.129	5.99	6.9	X-Shooter	K18	084.B-0499
NGC 3115	151.308	−7.719	10.866	7.18	−2.9	X-Shooter	Un	097.B-0435
NGC 3621	169.569	−32.814	9.739	7.0	6.9	X-Shooter	K18	086.B-0651
NGC 5068	199.728	−21.039	9.479	6.22	6.0	X-Shooter	Un	097.B-0435
NGC 5102	200.490	−36.630	9.32	7.86	−2.8	X-Shooter	K18	086.B-0651
NGC 5206	203.433	−48.151	9.361	7.18	−2.9	X-Shooter	K18	084.B-0499
NGC 5236	204.254	−29.865	10.579	7.38	5.0	X-Shooter	Un	097.B-0435
NGC 628	24.174	15.784	10.223	7.06	5.2	X-Shooter	Un	098.B-0024
NGC 7713	354.062	−37.938	8.808	5.61	6.7	X-Shooter	Un	097.B-0435
NGC 7793	359.458	−32.591	9.36	6.96	7.4	X-Shooter	K18	084.B-0499
VCC 0216	184.255	9.408	8.56	6.18	−2.5	FORS2	P11	078.B-0178
VCC 0308	184.712	7.862	9.112	6.49	−5.0	FORS2	P11	078.B-0178
VCC 0389	185.014	14.962	9.491	7.02	−3.6	FORS2	P11	078.B-0178
VCC 0490	185.412	15.745	9.100	6.76	−0.2	FORS2	P11	078.B-0178
VCC 0545	185.582	15.734	7.556	6.73	−2.2	FORS2	P11	078.B-0178
VCC 0592	185.712	13.593	7.909	6.05[a]	−5.0	FORS2	Un	085.B-0971
VCC 0725	186.101	15.075	7.33	6.02	−5.0	FORS2	P11	078.B-0178
VCC 0765	186.265	13.245	7.666	6.17[a]	−5.0	FORS2	Un	085.B-0971
VCC 0786	186.310	11.850	9.17	6.95[a]	−5.0	FORS2	Un	085.B-0971
VCC 0856	186.491	10.054	9.092	6.77	−5.0	FORS2	P11	078.B-0178
VCC 0871	186.524	12.560	7.467	5.54[a]	−5.0	FORS2	Un	085.B-0971
VCC 0916	186.638	12.743	8.876	6.50	−5.0	FORS2	Un	085.B-0971
VCC 0929	186.669	8.436	7.405	7.28	−0.8	FORS2	P11	078.B-0178
VCC 0940	186.696	12.454	9.143	6.7	−5.0	FORS2	Un	085.B-0971
VCC 0965	186.763	12.561	8.565	6.6	−5.0	FORS2	Un	085.B-0971
VCC 0990	186.821	16.024	9.186	6.83	−3.7	FORS2	P11	078.B-0178
VCC 1069	187.027	12.898	8.222	6.1	−5.0	FORS2	Un	085.B-0971
VCC 1073	187.036	12.093	9.21	6.7	−4.2	FORS2	Un	085.B-0971
VCC 1104	187.117	12.824	8.659	6.2	−5.0	FORS2	Un	085.B-0971
VCC 1122	187.174	12.916	8.78	6.5	−1.7	FORS2	Un	085.B-0971
VCC 1167	187.311	7.878	8.72	7.03	−5.0	FORS2	P11	078.B-0178
VCC 1185	187.348	12.451	8.424	6.19	−5.0	FORS2	P11	078.B-0178
VCC 1254	187.521	8.073	8.012	7.04	−5.0	FORS2	P11	078.B-0178
VCC 1261	187.543	10.779	9.64	6.66	−4.8	FORS2	P11	078.B-0178
VCC 1304	187.666	15.130	8.67	6.93	−2.2	FORS2	P11	078.B-0178
VCC 1308	187.691	11.343	8.232	6.35	−5.0	FORS2	P11	078.B-0178
VCC 1333	187.755	7.723	8.04	6.7	−5.0	FORS2	P11	078.B-0178
VCC 1348	187.816	12.332	8.836	7.33	−5.0	FORS2	P11	078.B-0178
VCC 1353	187.831	12.738	8.02	6.4	−4.4	FORS2	P11	078.B-0178
VCC 1355	187.834	14.115	8.931	6.08	−5.0	FORS2	P11	078.B-0178
VCC 1386	187.964	12.657	9.096	6.50	−4.9	FORS2	Un	085.B-0971
VCC 1389	187.967	12.482	8.125	6.49	−5.0	FORS2	P11	078.B-0178
VCC 1407	188.011	11.890	8.785	6.29	−5.0	FORS2	P11	078.B-0178
VCC 1431	188.097	11.263	9.204	6.63	−4.7	FORS2	Un	085.B-0971
VCC 1491	188.308	12.858	8.823	5.9	−3.7	FORS2	Un	085.B-0971
VCC 1661	189.103	10.385	8.36	6.47	−5.0	FORS2	P11	078.B-0178
VCC 1826	190.047	9.896	8.584	6.59	−5.0	FORS2	P11	078.B-0178
VCC 1861	190.244	11.184	8.959	6.51	−4.9	FORS2	P11	078.B-0178
VCC 1945	190.725	11.438	8.73	6.67	−2.2	FORS2	P11	078.B-0178
VCC 2019	191.335	13.693	9.004	6.78	−4.2	FORS2	P11	078.B-0178
Circinus	213.291	−65.339	10.485	7.569	3.3	MUSE	Un	0103.B-0396
ES O59-01	112.826	−68.188	7.896	6.16	9.8	MUSE	F22	0108.B-0904
FCC 119	53.391	−33.573	9.047	6.81	−2.9	MUSE	F21	296.B-5054
FCC 148	53.820	−35.266	9.883	8.37	−2.2	MUSE	F21	296.B-5054
FCC 153	53.879	−34.447	9.88	7.29	−2.1	MUSE	F21	296.B-5054
FCC 170	54.132	−35.295	10.543	8.45	−2.1	MUSE	F21	296.B-5054
FCC 177	54.198	−34.740	9.992	7.83	−1.9	MUSE	F21	296.B-5054
FCC 182	54.226	−35.375	9.505	6.03	−2.8	MUSE	F21	296.B-5054
FCC 188	54.269	−35.591	8.89	6.85	−4.3	MUSE	F21	096.B-0399
FCC 190	54.287	−35.195	9.995	7.18	−2.8	MUSE	F21	296.B-5054
FCC 193	54.299	−35.746	10.501	8.15	−2.8	MUSE	F21	296.B-5054

Table 1
(Continued)

(1) Name -	(2) R.A.(J2000) (deg)	(3) Decl.(J2000) (deg)	(4) $\log(M_{\rm host}/M_{\odot})$	(5) $\log(M_{\rm NSC}/M_{\odot})$	(6) Hubble Type -	(7) Instrument -	(8) Source -	(9) PID -
FCC 202	54.527	−35.440	9.137	6.76	−3.0	MUSE	F21	094.B-0895
FCC 207[b]	54.580	−35.129	8.68	6.06	−4.3	MUSE	J20	094.B-0576
FCC 211	54.590	−35.259	8.942	6.7	−4.5	MUSE	F21	096.B-0399
FCC 215	54.657	−35.758	6.79	5.94	−3.5	MUSE	F21	096.B-0399
FCC 222	54.805	−35.371	7.431	6.45	−2.2	MUSE	F21	096.B-0399
FCC 223	54.831	−35.726	8.78	6.38	−4.9	MUSE	F21	096.B-0399
FCC 227	54.959	−35.523	6.73	6.06	−3.5	MUSE	F21	096.B-0399
FCC 245	55.141	−35.023	8.77	6.05	−4.3	MUSE	F21	101.C-0329
FCC 249	55.175	−37.511	10.106	6.93	−4.9	MUSE	F21	296.B-5054
FCC 255	55.265	−33.779	9.648	6.98	−2.1	MUSE	F21	296.B-5054
FCC 277	55.595	−35.154	9.786	7.22	−2.9	MUSE	F21	296.B-5054
FCC 301	56.265	−35.973	9.662	6.91	−3.3	MUSE	F21	296.B-5054
FCC 306	56.439	−36.347	7.426	6.13	7.9	MUSE	J20	296.B-5054
FCC 310	56.557	−36.696	10.01	7.81	−1.9	MUSE	F21	296.B-5054
FCC 47	51.634	−35.714	9.926	8.74	−3.0	MUSE	F21	060.A-9192
FCCB 1241	54.569	−35.508	8.13	5.48	−5.0	MUSE	F21	102.B-0455
IC 1959	53.302	−50.414	7.926	6.13	8.5	MUSE	F22	0108.B-0904
IC 5332	353.615	−36.101	9.866	6.842	6.8	MUSE	Un	1100.B-0651
KK 197	200.508	−42.535	6.993	6.04	10.0	MUSE	F20	0101.A-0193
KKs 58	206.503	−36.329	6.875	5.87	−3.7	MUSE	F20	0101.A-0193
NGC 1487	58.942	−42.368	8.95	6.01	7.2	MUSE	F22	0100.B-0116
NGC 1705	73.557	−53.361	8.207	6.75[a]	−2.7	MUSE	Un	094.B-0745
NGC 1796	75.677	−61.140	9.060	6.82	5.3	MUSE	F22	0108.B-0904
NGC 2835[b]	139.470	−22.355	9.528	6.61	5.0	MUSE	Un	098.B-0551
NGC 3274	158.071	27.669	8.472	5.632	6.7	MUSE	Un	0110.B-0125
NGC 3368	161.691	11.820	10.506	7.89[a]	2.1	MUSE	Un	0104.B-404
NGC 3489	165.077	13.901	10.27	7.83[a]	−1.2	MUSE	Un	0104.B-404
NGC 3593	168.654	12.818	10.27	7.22	−0.4	MUSE	Un	0106.B-0359
NGC 4592	189.828	−0.532	9.02	5.8	8.0	MUSE	F22	095.B-0532
NGC 5253	204.983	−31.640	8.645	5.512	8.9	MUSE	Un	094.B-0745
NGC 853	32.922	−9.306	9.3	6.305	8.7	MUSE	F22	0108.B-0904
UGC 3755	108.466	10.522	7.75	4.777	9.9	MUSE	F22	0108.B-0904
UGC 5889	161.843	14.069	7.881	6.09	8.9	MUSE	F22	0108.B-0904
UGC 8041	193.803	0.117	8.83	6.74	6.9	MUSE	F22	0104.D-0503

Notes. Column (1): name of galaxy. Columns (2), (3): R.A., decl. (J2000) (from the NASA Extragalactic Database). Column (4): stellar mass of host galaxy; refer to K. Fahrion et al. (2021, 2022b), N. Hoyer et al. (2021), G. Consolandi et al. (2016), R. Pechetti et al. (2020), and N. C. Relatores et al. (2019). Column (5): stellar mass of NSC; refer to K. Fahrion et al. (2020, 2021, 2022b), N. Kacharov et al. (2018), C. Spengler et al. (2017), A. W. Graham & L. R. Spitler (2009), N. Hoyer et al. (2023a, 2023b), D. D. Nguyen et al. (2018, 2022), R. Sánchez-Janssen et al. (2019), S. G. Carlsten et al. (2022), R. Pechetti et al. (2020), I. Y. Georgiev et al. (2016), and D. Calzetti et al. (2015). Column (6): Hubble morphological type (G. de Vaucouleurs et al. 1991), with negative numbers assigned to early-type galaxies and positive numbers to late-type galaxies; refer to E. Kourkchi & R. B. Tully (2017). Column (7): instruments. Column (8): source paper of these nucleated galaxies (P11: S. Paudel et al. 2011; K18: N. Kacharov et al. 2018; J20: E. J. Johnston et al. 2020; F20: K. Fahrion et al. 2020; F21: K. Fahrion et al. 2021; F22: K. Fahrion et al. 2022a; Un: unpublished for NSCs research).

[a] Due to lack of literature data, the stellar masses of NSCs in NGC 1705, NGC 2784, NGC 3368, NGC 3489, VCC 0592, VCC 0765, VCC 0786, and VCC 0871 are estimated from $(M/L)_V$ and integral V-band luminosity after correction for flux loss in the slit.

[b] We also use data from programmes 096.B-0063, 097.B-0761, and 098.B-0239 for FCC 207 and 1100.B-0651 for NGC 2835.

The X-Shooter spectra of 12 nucleated galaxies were taken through three observing programs (084.B-0499(C), 086.B-0651(C), and 097.B-0435(B)). Spectral modeling for six of the 12 NSCs was presented by N. Kacharov et al. (2018). These observations were carried out with an 11″ slit length for all the spectroscopic arms. The slit widths are 0.″8, 0.″7, and 0.″6 respectively for the UVB, VIS, and NIR arms. In this work, only the UVB ($R \sim 6700$) and VIS ($R \sim 11400$) data are used for analysis. The raw data are reduced with the ESO REFLEX X-Shooter pipeline (v.3.5.3), which performs bias subtraction, flat-field correction, order tracing, wavelength calibration, flux calibration, flexure compensation, sky subtraction with dedicated offset sky exposures, image combination, etc. The final products are rectified 2D spectra and error maps.

2.1.2. FORS2 Spectra

The FORS2 is a multimode optical instrument mounted at UT1 of VLT. Among the galaxies with available FORS2 spectra, 26 were observed through the multiobject mode and 14 through the long-slit mode. All the spectra were taken with a V300 grism, a wavelength coverage of 3300–11000 Å, a slit width of 1″, with a corresponding spectral resolution of ∼11 Å FWHM (at 5000 Å). S. Paudel et al. (2011) presented spectral

analysis for the 26 NSCs observed with the multiobject mode. The 14 long-slit spectra were acquired with a 40″ slit length. The reader is referred to S. Paudel et al. (2010) for more details about the observational layout and data reduction.

2.1.3. MUSE Spectra

MUSE is an integral field spectrograph mounted at UT4 of VLT. The MUSE data used here were taken in the wide-field mode of MUSE, which provides a $1' \times 1'$ field of view and a wavelength coverage of 4700–9300 Å. The spectra have a spectral resolution of ∼2.5 Å FWHM (at 7000 Å), with a small wavelength dependence (R. Bacon et al. 2017). The spatial sampling is $0\farcs2 \times 0\farcs2$ and the spectral sampling is 1.25 Å pixel^{-1}. The raw data are reduced with the ESO REFLEX MUSE pipeline (v.2.8.7), following the standard procedures. To keep our analysis of the MUSE spectra consistent with that of the long-slit spectra from X-Shooter and FORS2, we create an artificial slit across the NSC and extract a subcube of the central $1.''2 \times 40''$ region of the reduced MUSE data cube for each galaxy. The following analysis of MUSE data will be based on these subcubes.

2.2. Spectral Extraction of NSCs and Their Host

Spectra of the nuclear regions of our galaxies are mainly from the NSCs, but have a nonnegligible contribution from the underlying host stellar populations. Therefore, it is necessary to perform a subtraction of the underlying host light for a clean analysis of the NSCs. To this end, we follow a procedure similar to that of S. Paudel et al. (2011). Specifically, we take the following approach to obtain NSC spectra clean of host contamination.

At the typical distance of our galaxies, the NSCs are unresolved or at most marginally resolved by seeing-limited ground-based observations. Therefore, the spatial profile near the NSCs may be described by a superposition of a seeing-defined Gaussian profile (representing the NSCs) and a Sérsic profile (representing the underlying host). To perform the profile decomposition, we first collapse the 2D long-slit spectra in the wavelength direction to obtain a white-light spatial profile. Then, the white-light spatial profile is fitted with a combination of a Gaussian function and a Sérsic function. The Gaussian function is defined by the standard deviation σ and peak flux, and the Sérsic function is defined by Sérsic index n, effective radius (R_e), and central surface brightness. After obtaining the best-fit parameters, the relative flux contribution of the Sérsic host to the nuclear region can be quantified. Our profile decomposition suggests that the local flux ratio of the Gaussian component to the Sérsic component falls well below 0.1 at radius $R > 4\sigma$. Therefore, we consider the region beyond 4σ (and $<6\sigma$) to be representative of the underlying host of NSCs, and restrict the spectral extraction of NSCs to the $R < 2\sigma$ region. In particular, a scaling factor C is first calculated by using the best-fit Sérsic component:

$$C = \frac{\int_0^{2\sigma} f_{\rm Sersic}\, dR}{\int_{4\sigma}^{6\sigma} f_{\rm Sersic}\, dR}. \quad (1)$$

Then, NSC spectra that are clean of host contamination can be obtained as follows:

$$f_\lambda^{\rm NSC} = \int_0^{2\sigma} f_{\lambda,R}^{\rm obs}\, dR - C \times \int_{4\sigma}^{6\sigma} f_{\lambda,R}^{\rm obs}\, dR, \quad (2)$$

where $f_{\lambda,R}^{\rm obs}$ is the observed flux density at given wavelength λ and radius R. As described above, the spectra of the representative host underlying NSCs can be simply derived as

$$f_\lambda^{\rm host} = \int_{4\sigma}^{6\sigma} f_{\lambda,R}^{\rm obs}\, dR. \quad (3)$$

Note that, in the above calculation, we have assumed that the scale factor C does not vary with wavelength. A wavelength-dependent solution for C is preferable, but it would be subject to significant uncertainties in practice, due to a lower signal-to-noise ratio (S/N).

Lastly, all of the NSC spectra and host spectra are corrected for Galactic extinction by using the Python packages SFDMAP (D. J. Schlegel et al. 1998) and EXTINCTION (K. Barbary 2016), assuming the J. A. Cardelli et al. (1989) extinction law with $R_v = 3.1$.

3. Analysis

3.1. Full-spectrum Fitting

We fitted all spectra by using the full-spectrum fitting technique with the Python package Penalized Pixel-Fitting (or pPXF; M. Cappellari & E. Emsellem 2004; M. Cappellari 2017), which is a well developed tool for extracting stellar population properties and kinematics by fitting weighted combinations of single stellar population (SSP) models to an observed spectrum, without a prior assumption about the functional form of the star formation history. In this work, we adopt MILES SSP model spectra (A. Vazdekis et al. 2010), which are generated based on the MILES spectral library, the BaSTi scaled-solar isochrones, and a Kroupa initial stellar mass function. The SSP models cover a range of ages from 0.03 Gyr to 14 Gyr and a range of metallicities [M/H] from −2.27 to +0.40. The model spectra have a spectral resolution of 2.51 Å in the wavelength range from 3525 to 7500 Å. Our spectral fitting is performed over the wavelength range from 4000 to 6800 Å for the X-Shooter and FORS2 data, and from 4700 to 6800 Å for the MUSE data. To keep the analysis consistent for different data sets, the X-Shooter and MUSE spectra (and the model spectra) are smoothed to the same spectral resolution of ∼11 Å of the FORS2 data prior to the spectral modeling. We follow a procedure similar to Y. Tang et al. (2022) to carry out the pPXF fitting.

(i) First, we fit each spectrum for redshift and velocity dispersion by invoking additive and multiplicative polynomials of degree 10 to accommodate the difference in continuum shape between models and observations. With the above fitting, the line-of-sight velocity and the velocity dispersion are determined and fixed in the subsequent fitting.

(ii) Second, with the kinematic parameters being fixed, we perform a second pPXF fitting to each spectrum without regularization, by invoking multiplicative polynomials to adjust the continuum of the models. The resultant polynomial parameters define a correction curve that accounts for flux calibration inaccuracy and internal dust

reddening. In this round of fitting, the noise spectrum is rescaled such that the minimum reduced χ^2_r is equal to 1. The correction curve, rescaled noise spectrum, and residual spectrum between the best-fit model and data are used in the following fitting.

(iii) Third, we fit for stellar age and [M/H] via a wild bootstrapping method (R. Davidson & E. Flachaire 2008), where we add generated noise (–noise or noise with probability = 0.5) to the observed spectrum according to the residual spectrum derived above 100 times, and perform pPXF fitting to each of the noise-disturbed spectra by invoking a mild regularization (regul = 10). The 100 fittings result in distributions for best-fit light- and mass-weighted ages and [M/H]. These distributions are used determine the most probable values of ages, [M/H], and their associated 68% confidence intervals. The results for our sample are presented in Table 3.

3.2. [α/Fe] Estimation

α elements are primarily produced in short-lived high-mass stars ($\gtrsim$8 $M_\odot$) and are released via core-collapse supernovae, whereas for the Fe-peak elements, both core-collapse supernovae and thermonuclear supernovae make significant contributions (thermonuclear supernovae contribute the most). Therefore, the relatively longer delay times of thermonuclear supernovae ($\gtrsim$1 Gyr) than core-collapse supernovae result in a higher [α/Fe] ratio for stellar systems formed earlier or over shorter timescales (e.g., D. Thomas et al. 2003).

To estimate [α/Fe] for our sample, we follow D. Thomas et al. (2003) and take the Lick absorption-line index Mg*b* as a proxy for α elements and the composite Fe Lick index ⟨Fe⟩ (= (Fe5270 + Fe5335)/2) as a proxy for Fe-peak elements. We adopt the semiempirical MILES stellar population models with variable [α/Fe] (A. T. Knowles et al. 2023), which provide a uniform coverage of [α/Fe] from −0.2 to +0.6. As with our full-spectrum fitting, we choose the Kroupa initial mass function and smooth the model spectra to a resolution of 11 Å. To measure the Lick indices (Mg*b*, Fe5270, Fe5335) on both the model and observed spectra, we use the Python-based package PYPHOT (M. Fouesneau 2022). There is a weak but nonnegligible dependence of the Mg*b*/⟨Fe⟩ ratio on stellar age and metallicity. Therefore, for each NSC or host spectrum, we only consider models that match the light-weighted age obtained from our full-spectrum fitting, and obtain the [α/Fe] values through interpolation of the model grids with respect to the [α/Fe] parameter. For a small number of index measurements that fall outside the model grids, we estimate the [α/Fe] values through a linear extrapolation. The uncertainties of [α/Fe] are determined by randomly disturbing the measured index values according to the measurement uncertainties and repeating the above procedure of [α/Fe] estimation.

The distribution of the NSCs and circum-NSC host on the Mg*b* versus ⟨Fe⟩ diagram is shown in Figure 1, where model grids of different [α/Fe] at three representative ages are overlaid for illustration. In Figure 1, the small filled circles and hollow circles represent the measured indices of NSCs and underlying hosts, respectively. A small number of spectra (12 NSCs and three hosts) have negative values for one of the two Fe Lick indices, which may be attributed to remarkable noise disturbance. In this case, only the Fe index with positive measurement is used in the estimation of [α/Fe] based on model grids involving only a single Fe Lick index. Lastly, we

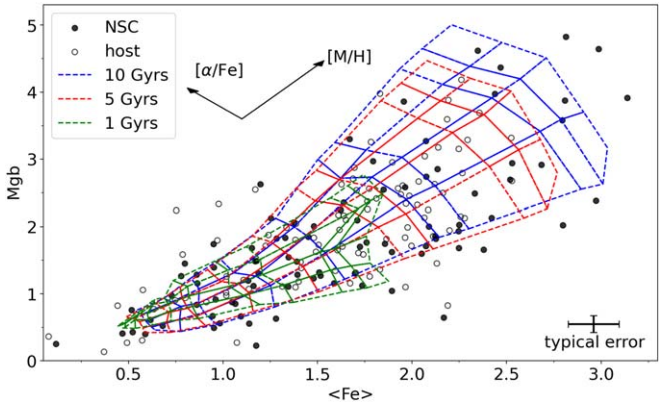

Figure 1. Mg*b*–⟨Fe⟩ index diagram. Measurements of both the NSCs (filled circles) and underlying host (hollow circles) of our sample are plotted. The MILES SSP model grids for three different stellar ages (10 Gyr in blue, 5 Gyr in red, and 1 Gyr in green) are overlaid for illustration. In practice, the [α/Fe] parameter is estimated by interpolating the model grids for a given age (as obtained from the full-spectrum fitting). For the small number of measurements falling outside the model grids, [α/Fe] is estimated through a linear extrapolation of the model grids.

note that the spectra of 10 galaxies are corrupted near the wavelength range that defines Mg*b* or both of the two Fe indices, so we ignore those 10 galaxies whenever the [α/Fe] parameter is relevant in the following analysis.

3.3. Comparison with Measurements in the Literature

Here we compare our light-weighted result of age and [M/H] with the results in the literature, which are from S. Paudel et al. (2011), N. Kacharov et al. (2018), and K. Fahrion et al. (2021, 2022b). The comparisons for age and [M/H] are respectively shown in the upper and lower panels of Figure 2. It is worth noting that the spectral extraction and stellar population modeling in the literature are significantly different from ours. In particular, S. Paudel et al. (2011) estimated the stellar population parameters based on Lick indices, instead of full-spectrum fitting as adopted in our work. N. Kacharov et al. (2018) and K. Fahrion et al. (2022b) did not subtract the flux contamination of the underlying hosts in the NSC spectra.

In Figure 2, we show that our [M/H] estimations are in reasonable agreement with the literature values. The results for age appear to have a substantial difference for many NSCs, especially when compared to those based on Lick indices. This comparison may partially reflect the fact that [M/H] is better constrained by the integrated-light spectra than ages, and also demonstrates the potential problem of statistical analysis of stellar population properties based on a direct compilation of estimates from the literature.

3.4. Sample Classification Based on the Projected Phase-space Diagram

To explore the environmental dependence of NSC properties, we turn to the projected phase-space diagram. The projected phase-space diagram for a cluster of galaxies involves the projected distance to the cluster center and the line-of-sight velocity of individual galaxies relative to the cluster. Recent simulations (e.g., J. Rhee et al. 2017; R. Smith et al. 2019) suggest that the location of a galaxy in the projected phase-space diagram is, in a statistical sense, an indicator of the infall time and thus the effect of the

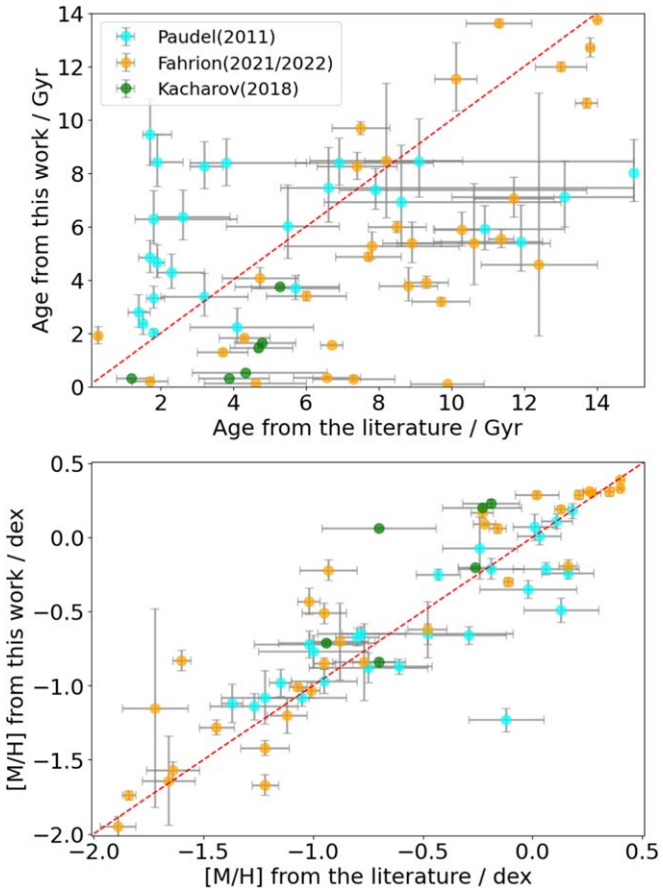

Figure 2. Comparison of ages (top) and [M/H] (bottom) of the NSCs from the literature and this work. The red dashed lines indicate the one-to-one relation.

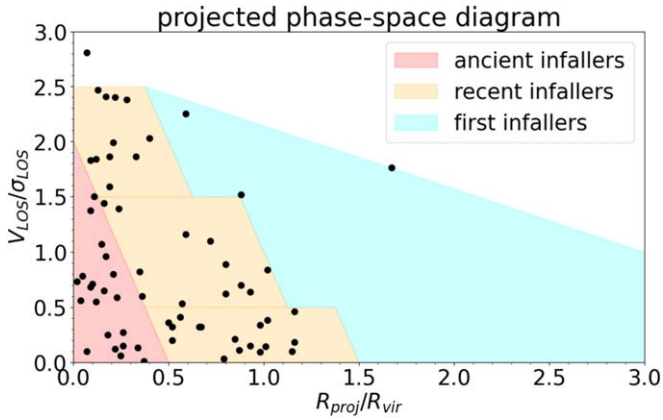

Figure 3. Projected phase-space diagram, being used to classify our galaxies into different environment. Each black dot is a galaxy associated with the Virgo or Fornax cluster in our sample. *x*-axis: the projected distance of a galaxy from the cluster center normalized by the virial radius of the cluster. *y*-axis: the line-of-sight velocity difference between the galaxy and the cluster center normalized by the velocity dispersion of the cluster. The projected phase-space diagram is split into three color-coded regions, i.e., first infallers, recent infallers and ancient infallers, largely following J. Rhee et al. (2017). Note that galaxies in Local Volume are not shown here.

environment on the evolution of the galaxies in question. Many of our galaxies are associated with the two nearest galaxy clusters: Virgo and Fornax. The distribution of our galaxies on the projected phase-space diagram is shown in Figure 3, where the projected distance and line-of-sight velocities with respect to the cluster center have been normalized, respectively, by the virial radius and velocity dispersion of the host cluster.

The demarcation lines for phase-space regions occupied by galaxies with distinct infall times in a statistical sense from J. Rhee et al. (2017) are also plotted in Figure 3. Following J. Rhee et al. (2017), we classify the cluster galaxies in our sample broadly into three subsamples as indicated by the regions filled with different colors in Figure 3, i.e., first infallers, recent infallers, and ancient infallers, where the first infallers refer to galaxies that are falling toward the virial radius for the first time, the recent infallers refer to galaxies that have crossed the virial radius in the last couple of Gyr, and the ancient infallers refer to galaxies that are close to being virialized in the cluster. In what follows, we will group the galaxies not associated with the two galaxy clusters in our sample into the above defined subsample of first infallers and redefine them as Local Volume (LV) or first infallers.

4. Results

4.1. Mass–Metallicity Relation

The mass–metallicity distributions of our sample are presented in Figure 4, where the left panel plots [M/H] of NSCs and their host as a function of the galaxy stellar mass and the right panel plots [M/H] as a function of the NSC stellar mass. To guide the eye, a constrained B-spline smooth curve fitting for the 50% (median) quantile of the [M/H] distribution of NSCs (solid line) and circum-NSC host (dashed line) is performed by using the CRAN package "cobs." In addition, the linear relations between mean metallicities of GCs and the host galaxy stellar mass, as obtained by E. W. Peng et al. (2006), are also overplotted in the left panel. We note that the E. W. Peng et al. (2006) relations were calibrated based on the metallicity scale of R. Zinn & M. J. West (1984), which, although being referred to as [Fe/H], has been shown to trace the total metallicity rather than iron abundance (D. Thomas et al. 2003).

The NSC metallicities have a significant correlation with their host galaxy mass, with the Pearson correlation coefficient $r = 0.73$ (P-value $= 2.1 \times 10^{-17}$), whereas the NSC metallicities have a weaker correlation with the NSC mass ($r = 0.60$). The NSCs have systematically lower average metallicities than the host at $\log M_{\rm host} \lesssim 9$ ($M_{\rm host}$ is in units of $M_\odot$ throughout), whereas the reverse is true at higher galaxy stellar masses. We will explore the metallicity difference between NSCs and their host in more detail in the next subsection.

In comparison to GCs, the metallicities of NSCs exhibit a steeper overall dependence on galaxy mass, particularly at $\log M_{\rm host} \lesssim 9.5$. Compared to the blue GCs, NSCs have systematically higher metallicities (with few exceptions) across the range of galaxy stellar mass explored here. At $\log M_{\rm host} \lesssim 8.5$, NSCs have average metallicities slightly lower than typical red GCs for given galaxy stellar mass, while at $\log M_{\rm host} > 8.5$, NSCs have increasingly higher metallicities than typical red GCs toward the higher galaxy mass end.

Based on the above results, we can already infer that inspiral–merger of classical GCs cannot be an important formation channel for NSCs residing in galaxies of $\log M_{\rm host} \gtrsim 9$, confirming previous claims based on much smaller samples and inhomogeneous estimation. In contrast, typical NSCs in galaxies with $\log M_{\rm host} \lesssim 8.5$ were probably formed at a similar or even an earlier epoch than their typical red GCs, prior to the formation of the bulk of their circum-NSC

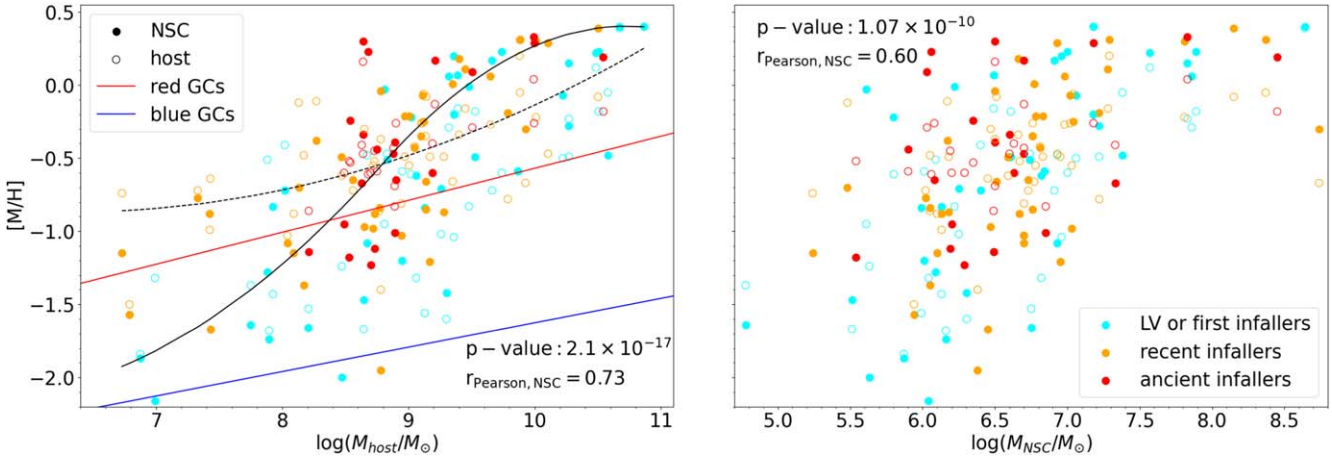

Figure 4. Mass–metallicity distribution of the NSCs and the host. The [M/H] of NSCs and the circum-NSC host is plotted against the galaxy stellar mass in the left panel and against the NSC stellar mass in the right panel. In both panels, the NSCs are represented as filled circles, while the host is represented as open circles. The data points are color-coded according to the projected classification by phase-space environment, as indicated in the right panel and illustrated in Figure 3. The black solid line and black dashed line respectively represent constrained B-spline smooth curve fittings for the 50% (median) quantile of [M/H] of NSCs and the circum-NSC host. According to E. W. Peng et al. (2006), the red line and blue line represent mean metallicities of red GC populations and blue GC populations as a function of galaxy stellar mass.

host stellar populations. Therefore, GC inspiral–merger is probably the dominant formation channel for NSCs in galaxies of $\log M_{\rm host} \lesssim 8.5$. In a similar vein, NSCs in galaxies of intermediate stellar masses may have a mixed formation mechanism, involving both GC inspiral–merger and in situ star formation.

4.2. The Metallicity Difference between NSCs and Their Host

As is evident in Figure 4, typical GCs have metallicities lower than the circum-NSC host across the galaxy stellar mass range explored here, so NSCs that have lower metallicities than the underlying host are expected to form through inspiral–merger of metal-poor star clusters. On the other hand, if the growth of NSCs is sustained by continuous gas inflow from large galactocentric radii, the inflowing gas is expected to be progressively metal-enriched as it flows through the disk or halo. So NSCs formed in situ over extended timescales may have comparable or even higher metallicities than the circum-NSC host.

In Figure 5, the metallicity differences $[{\rm M/H}]_{\rm NSC} - [{\rm M/H}]_{\rm host}$ (hereafter $[{\rm M/H}]_{\rm diff}$) are plotted against the galaxy stellar mass, where the data points in different panels are color-coded by various light-weighted stellar population properties: metallicity of host galaxies, metallicity of NSCs, age of NSCs, age of the circum-NSC host, [α/Fe] of NSCs, and stellar mass of NSCs.

Noting the overall trend of $[{\rm M/H}]_{\rm diff}$ versus $M_{\rm host}$, there is virtually no dependence of $[{\rm M/H}]_{\rm diff}$ on galaxy mass at $\log M_{\rm host} \lesssim 8.5$, where the average $[{\rm M/H}]_{\rm diff}$ is ~ -0.3 with a substantial scatter. Nearly all galaxies with $\log M_{\rm host} \lesssim 8.5$ have $[{\rm M/H}]_{\rm diff} < 0$. In contrast, at the high-galaxy-mass end of $\log M_{\rm host} \gtrsim 9.5$, nearly all galaxies have $[{\rm M/H}]_{\rm diff} \geqslant 0$. Galaxies in the intermediate-mass range of 8.5–9.5 have average $[{\rm M/H}]_{\rm diff} \sim 0.0$, with comparable numbers of galaxies above and below the average. Moreover, the average $[{\rm M/H}]_{\rm diff}$ appears to follow a unimodal distribution as a function of $\log M_{\rm host}$, with a peak of average $[{\rm M/H}]_{\rm diff} \sim 0.5$ near $\log M_{\rm host} \sim 9.8$. The average $[{\rm M/H}]_{\rm diff}$ drops steadily toward both the lower-mass end (until reaching below $\log M_{\rm host} \sim 8.5$) and higher-mass end, reaching $[{\rm M/H}]_{\rm diff} \sim 0$ at $\log M_{\rm host} \sim 11$.

We note that the peak of the average $[{\rm M/H}]_{\rm diff}$ distribution is at a higher galaxy mass than the well-known unimodal dependence of nucleation fraction on galaxy mass, which peaks near $\log M_{\rm host} \sim 9.0$ (e.g., N. Hoyer et al. 2021) where the average $[{\rm M/H}]_{\rm diff} \sim 0$. We also note that the large metallicity difference between NSCs and the circum-NSC host cannot be explained by the well-established negative radial metallicity gradients of galaxies, which predict $[{\rm M/H}]_{\rm diff}$ values well below 0.1 dex.

To understand the drivers of the spread of $[{\rm M/H}]_{\rm diff}$, we explore various stellar population properties in different panels of Figure 5. By comparing panels (a) and (b), we find that galaxies with positive $[{\rm M/H}]_{\rm diff}$ have systematically more metal-enriched NSCs than galaxies with negative $[{\rm M/H}]_{\rm diff}$. Looking more closely at the dependence of $[{\rm M/H}]_{\rm diff}$ on galaxy mass, the large spread of $[{\rm M/H}]_{\rm diff}$ at intermediate galaxy masses ($8.5 \lesssim \log M_{\rm host} \lesssim 9.5$) is primarily attributed to the spread of $[{\rm M/H}]_{\rm NSC}$, whereby galaxies with larger $[{\rm M/H}]_{\rm diff}$ tend to have larger $[{\rm M/H}]_{\rm NSC}$ rather than smaller $[{\rm M/H}]_{\rm host}$. In contrast to the intermediate-mass galaxies, the spread in $[{\rm M/H}]_{\rm diff}$ at $\log M_{\rm host} \gtrsim 9.5$ is primarily attributed to the spread of $[{\rm M/H}]_{\rm host}$ rather than $[{\rm M/H}]_{\rm NSC}$, whereby galaxies with larger $[{\rm M/H}]_{\rm diff}$ tend to have lower $[{\rm M/H}]_{\rm host}$, with a remarkable scatter. In addition, stellar age is not closely correlated with the spread of $[{\rm M/H}]_{\rm diff}$, except that most NSCs (80%) with $[{\rm M/H}]_{\rm diff} > 0.5$ have relatively young NSC ages ($\leqslant$5 Gyr; panel (d)). Lastly, neither [α/Fe] (panel (e)) nor $M_{\rm NSC}$ (panel (f)) is correlated with the spread in $[{\rm M/H}]_{\rm diff}$ at given galaxy stellar mass.

The above findings suggest that the connection between metal enrichment of NSCs and their underlying host is dependent on galaxy stellar mass. In particular, it is only for intermediate-mass galaxies that the metal enrichment level of NSCs largely drives the spread of $[{\rm M/H}]_{\rm diff}$. In contrast, in the high-galaxy-mass regime, the metal enrichment level of NSCs appears to be largely "saturated," albeit with substantial scatter, and galaxies with larger $[{\rm M/H}]_{\rm diff}$ tend to have lower $[{\rm M/H}]_{\rm host}$, which is probably attributed to low-metallicity gas inflow toward the circum-NSC host region. In addition, it is intriguing that more metal-enriched NSCs in intermediate-mass galaxies tend not to have larger NSC mass. This implies a lack

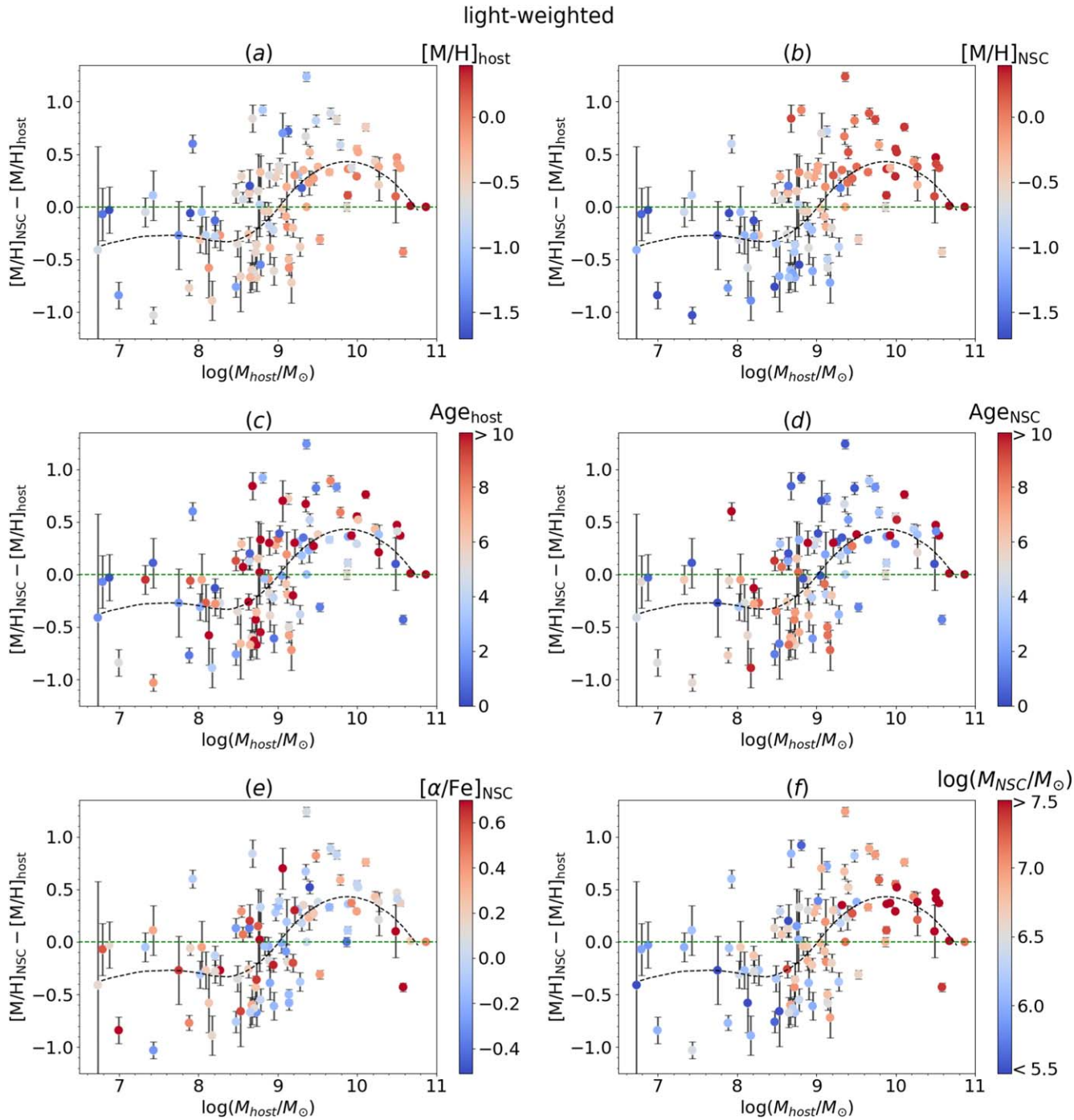

Figure 5. Metallicity difference of NSCs and circum-NSC host ($[M/H]_{NSC} - [M/H]_{host}$) vs. host galaxy stellar mass. The data points are color-coded by different stellar population properties in different panels, as indicated in the title of each color bar. The green dashed horizontal line in each panel marks zero metallicity difference. In each panel, a constrained B-spline smooth curve fitting for the 50% (median) quantile of $[M/H]_{NSC} - [M/H]_{host}$ is represented by a black dashed curve.

of synchrony between metal enrichment and mass growth of NSCs.

4.3. Age–Metallicity Distributions

The age–metallicity relation is a powerful probe of the evolutionary history of stellar systems. The age–[M/H] distributions of our sample are presented in Figure 6, where the galaxies/NSCs are distinguished according to $[M/H]_{diff}$, galaxy stellar mass, age of the circum-NSC host, [α/Fe] of the NSCs, and logM_{NSC}.

The subsamples of NSCs with $[M/H]_{diff} < 0$ and > 0 have distinct age–[M/H] distributions. Specifically, a majority of NSCs with $[M/H]_{diff} < 0$ are clustered within a narrow age interval centered near ∼7 Gyr and a narrow $[M/H]_{NSC}$ interval between −1.1 and −0.5. Except for this clustering trend, there is no obvious age–[M/H] correlation for NSCs with $[M/H]_{diff} < 0$. In contrast, NSCs with $[M/H]_{diff} > 0$ appear to consist of two major groups in the age–[M/H] diagram: one group of NSCs (∼25%) randomly occupy the old-age ($\gtrsim$7 Gyr) and high-[M/H] ($\gtrsim$−1.0) regime, and the other (dominant) group of NSCs (∼63%) run from the lower-[M/H] and older-

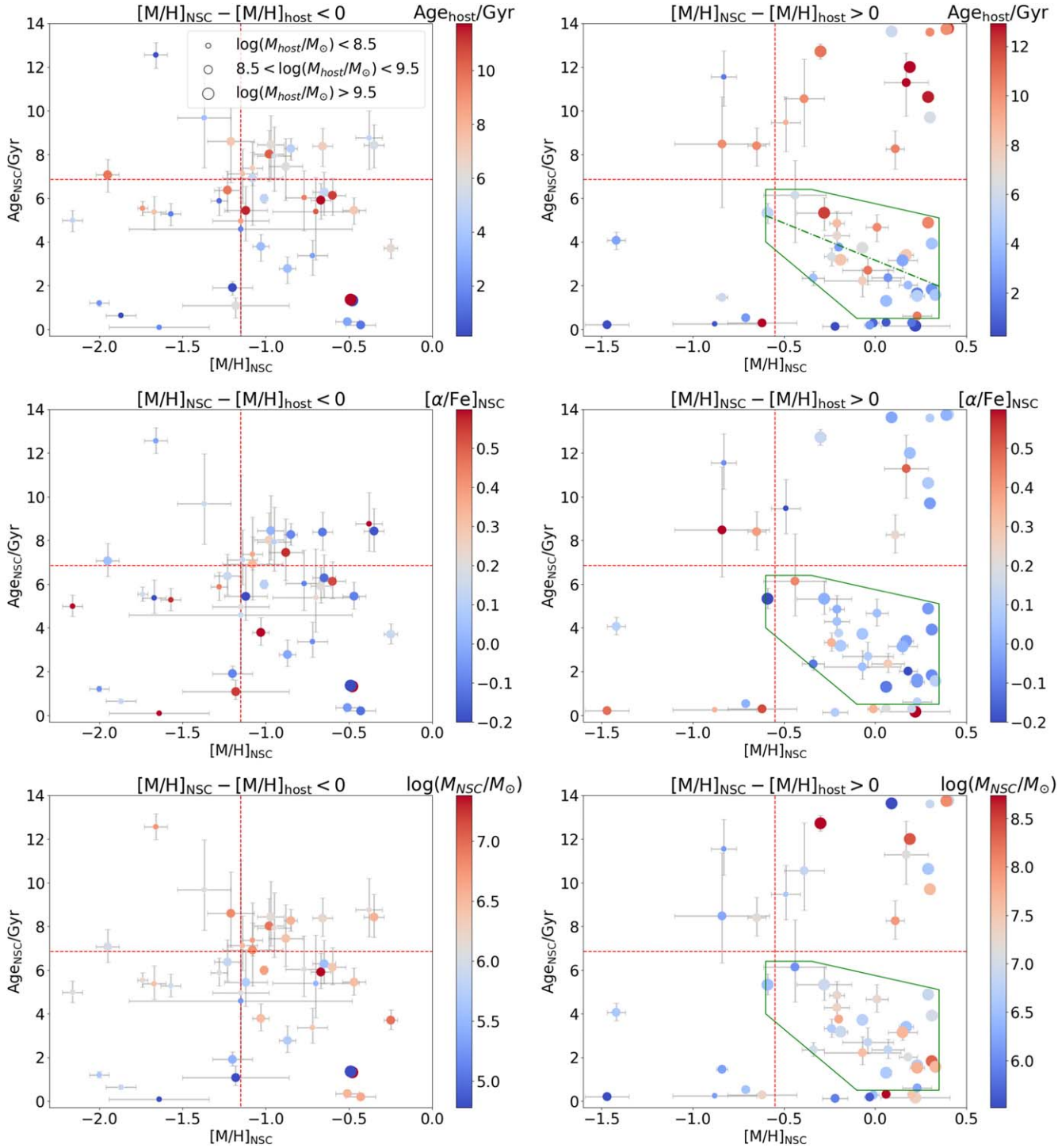

Figure 6. Age–metallicity distribution of NSCs with $[M/H]_{NSC} < [M/H]_{host}$ (left panels) and $[M/H]_{NSC} > [M/H]_{host}$ (right panels). The data points are color-coded according to the light-weighted Age_{host} (top row), $[\alpha/Fe]_{NSC}$ (middle row), and $\log M_{NSC}$ (bottom row). The symbol sizes are in accord with the ranges of host galaxy stellar mass, as indicated in the legend. The green solid polygon in the right panels encloses data points belonging to the same GMM group, and the green dashed–dotted line is the best-fit linear relation to NSCs enclosed by the green polygon. See Section 4.3 for details.

age corner to the higher-[M/H] and younger-age end (i.e., lower right quadrant), and particularly they exhibit a broad negative age–[M/H] correlation. About ∼12% of the NSCs with $[M/H]_{diff} > 0$ fall in the low-[M/H] and young-age quadrant of the diagram that cannot be assigned to the above two major groups. It is remarkable that all of the NSCs in this minority group have relative low stellar mass.

To verify the negative age–[M/H] correlation mentioned above, we perform a "Gaussian mixture model" (GMM) decomposition of the age–[M/H] distribution of NSCs with $[M/H]_{diff} > 0$, by utilizing the Python package SKLEARN. We find that most of the NSCs that constitute the visually identified dominant group belong to the same GMM cluster (data points enclosed by a green solid polygon in the right

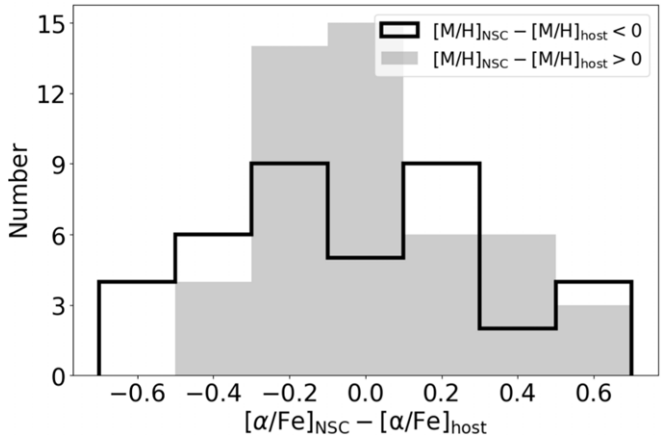

Figure 7. Distributions of $[\alpha/\mathrm{Fe}]$ difference between NSCs and the circum-NSC host. NSCs with $[\mathrm{M/H}]_{\mathrm{diff}} > 0$ and <0 are shown separately, as indicated in the legend.

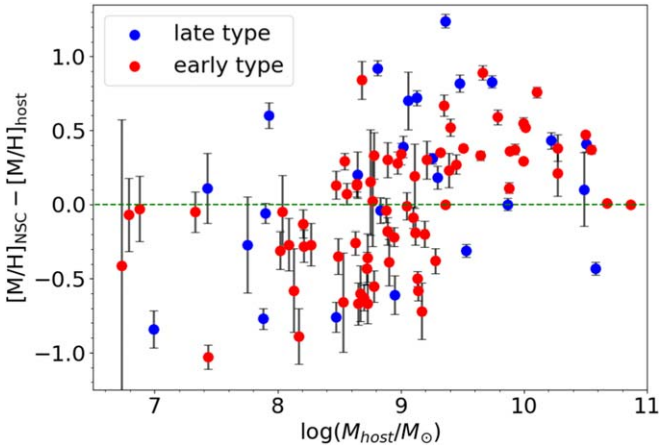

Figure 8. Similar to Figure 5, except that the data points are differentiated according to the Hubble types of the galaxies, with early types being plotted in red and late types in blue.

panels of Figure 6), which is distinct from the rest of the NSCs. We perform a linear least-squares fitting to this dominant GMM cluster of NSCs and overplot the best-fit relation (green dashed–dotted line). The corresponding Spearman rank correlation coefficient is −0.56, with a p-value of 0.0037, suggesting a significant negative correlation.

The age–$[\mathrm{M/H}]$ distributions are independent of galaxy stellar mass and NSC mass, except that most low-mass galaxies (i.e., $\log M_{\mathrm{host}} \lesssim 8.5$) fall into the subsample with $[\mathrm{M/H}]_{\mathrm{diff}} < 0$. The above-mentioned dominant group of NSCs with $[\mathrm{M/H}]_{\mathrm{diff}} > 0$ tend to have younger host ages and lower $[\alpha/\mathrm{Fe}]$ toward the higher-$[\mathrm{M/H}]$ end, albeit with substantial scatter, while the subdominant group of NSCs in the old-age, high-$[\mathrm{M/H}]$ quadrant mostly have relatively old host age and similarly low $[\alpha/\mathrm{Fe}]$ to the dominant group.

The negative age–metallicity relation for the majority of NSCs with $[\mathrm{M/H}]_{\mathrm{diff}} > 0$ is a reflection of extended period of self-enrichment of the NSCs in their host galaxies. Given the lack of synchrony between metal enrichment and mass growth already inferred in Section 4.2, it is not surprising that there is no systematic difference of M_{NSC} along the age–metallicity relation. In contrast, the lack of an age–metallicity relation for NSCs with $[\mathrm{M/H}]_{\mathrm{diff}} < 0$ may be attributed to an early assembly of NSCs over relatively short timescales. With that said, the small fraction of NSCs with $[\mathrm{M/H}]_{\mathrm{diff}} < 0$ and very young ages (i.e., $\lesssim$2 Gyr) may imply substantial in situ star formation in rare circumstances (S. Paudel & S.-J. Yoon 2020).

When gas inflow triggers in situ star formation in NSCs, the same inflow event should have triggered nearly synchronous star formation in the circum-NSC host regions. Therefore, we expect that NSCs that grow more or less in synchrony with the circum-NSC host should have similar $[\alpha/\mathrm{Fe}]$ (an indicator of metal enrichment timescales; see Section 3.2). The $[\alpha/\mathrm{Fe}]_{\mathrm{NSC}}$–$[\alpha/\mathrm{Fe}]_{\mathrm{host}}$ distributions of our sample are shown in Figure 7. As expected, the distribution of NSCs with $[\mathrm{M/H}]_{\mathrm{diff}} > 0$ is highly peaked near $[\alpha/\mathrm{Fe}]_{\mathrm{NSC}}$–$[\alpha/\mathrm{Fe}]_{\mathrm{host}} \sim 0.0$, whereas NSCs with $[\mathrm{M/H}]_{\mathrm{diff}} < 0$ have a much flatter distribution of $[\alpha/\mathrm{Fe}]_{\mathrm{NSC}}$–$[\alpha/\mathrm{Fe}]_{\mathrm{host}}$.

4.4. Dependence on Hubble Type of the Host Galaxies

Here we explore whether the stellar population properties of NSCs are related to the morphological type of the host galaxies. To this end, the $[\mathrm{M/H}]_{\mathrm{diff}}$–$\log M_{\mathrm{host}}$ distribution (Figure 8) and the $\mathrm{age}_{\mathrm{NSC}}$–$[\mathrm{M/H}]_{\mathrm{NSC}}$ distribution (Figure 9) are plotted by differentiating the host galaxies into early Hubble types (numerical Hubble type <0; S0/a or earlier) and late Hubble types (numerical Hubble type >0). Given the inhomogeneous nature of our sample, we do not attempt to perform a quantitative comparison of the distributions of different Hubble types in the explored parameter space; instead, we focus on the overall coverage of the parameter space and examine whether there is a systematic difference in NSC stellar populations between early and late types.

The sample is dominated by early-type hosts. However, the late types appear to cover a similar parameter space to the early types in the $[\mathrm{M/H}]_{\mathrm{diff}}$ versus $\log M_{\mathrm{host}}$ diagram. In the $\mathrm{age}_{\mathrm{NSC}}$ versus $[\mathrm{M/H}]_{\mathrm{NSC}}$ diagrams, it is remarkable that all of the NSCs with $[\mathrm{M/H}]_{\mathrm{diff}} > 0$ that occupy the lower-$[\mathrm{M/H}]$ and younger-age (lower-left) quadrant reside in late-type hosts with $\log M_{\mathrm{host}} < 9.5$, while all of the NSCs with $[\mathrm{M/H}]_{\mathrm{diff}} > 0$ that occupy the higher-$[\mathrm{M/H}]$ and older-age (upper-right) quadrant reside in early-type hosts. The rest of NSCs with $[\mathrm{M/H}]_{\mathrm{diff}} > 0$ in both early-type and late-type hosts appear to follow the negative age–$[\mathrm{M/H}]$ relation described in Section 4.3.

4.5. Dependence on Host Galaxy Environment

Here we explore the environmental dependence of the stellar population properties of NSCs. According to Section 3.4, our sample can be divided into subsamples based on the location in the projected phase space. Each galaxy in the sample is assigned to be one of the four environmental types of "ancient infallers," "recent infallers," "first infallers," and "LV" based on its location in the projected phase-space diagram.

We present the $[\mathrm{M/H}]_{\mathrm{diff}}$–$\log M_{\mathrm{host}}$ relation and $\mathrm{age}_{\mathrm{NSC}}$–$[\mathrm{M/H}]_{\mathrm{NSC}}$ diagrams by color-coding our galaxies according to their phase-space classifications in Figure 10 and Figure 11. Note that the LV and first infaller types are combined as "LV or first infallers." We find that different phase-space subsamples generally cover similar $[\mathrm{M/H}]_{\mathrm{diff}}$ ranges for given galaxy stellar mass in Figure 10, except that there is a lack of ancient infallers at $\log M_{\mathrm{host}} \lesssim 8.0$ in our sample. We also note that NSCs with the highest $[\mathrm{M/H}]_{\mathrm{diff}}$ values are mostly LV or first infallers. This apparent preference is probably due to the fact that the "LV or first infallers" sample is biased to late-type galaxies (Figure 8) with relatively young NSC ages (Figure 5). Given the heterogeneous nature of our sample, we do not

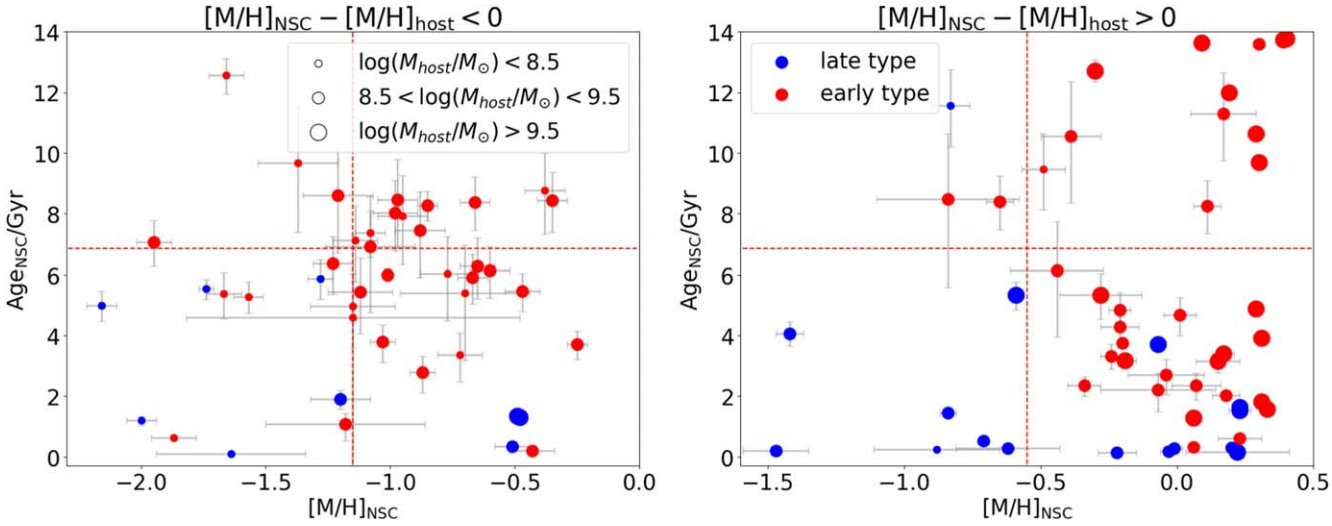

Figure 9. Similar to Figure 6, except that the data points are differentiated according to the Hubble types of the galaxies, with early types being plotted in red and late types in blue.

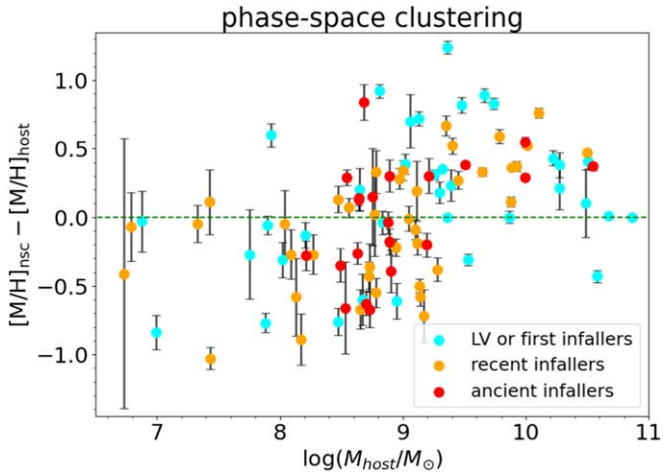

Figure 10. Similar to Figure 5, except that the sample is divided into subsamples according to the phase-space classification (see Figure 3 and Section 3.4).

attempt to further quantify the difference or similarity of different subsamples, but point out that no clear dependence on phase-space classifications is found in the $[M/H]_{diff}$–$\log M_{host}$ diagram.

5. Discussion

5.1. The Formation Mechanisms of NSCs Revealed by Stellar Population Studies

The plausible formation mechanisms of NSCs proposed in the literature broadly fall into two categories: (1) dynamical-friction-driven inspiral and merger of either classical GCs or young star clusters and (2) in situ star formation (e.g., N. Neumayer et al. 2020). It is generally thought that in situ star formation may be the dominant mechanism for relatively high-mass galaxies ($\log M_{host} \gtrsim 9$), while infall and mergers of star clusters may be more important for low-mass galaxies ($\log M_{host} < 9$). The theoretical models by F. Antonini et al. (2015) took into consideration in situ star formation, the GC infall process, as well as the tidal influence of a central massive black hole on NSCs and presented a coevolution picture of NSCs, black holes, and host galaxies. F. Antonini et al. (2015) found that for most host galaxies, the mass fraction of NSCs formed by in situ star formation can be ∼40%. The models reproduced the decreasing nucleation fraction at the high-galaxy-mass end but failed to explain the observed decrease of nucleation fraction toward the low-galaxy-mass end (R. Sánchez-Janssen et al. 2019). S. Paudel et al. (2011) analyzed spectra of 26 nucleated dE galaxies in the Virgo cluster and found most of their NSCs are significantly younger than galactic main bodies, with an average age difference of 3.5 Gyr, indicating gas accretion into NSCs. S. Paudel et al. (2011) also found fairly old and metal-poor NSCs in very faint dEs, resembling the properties of their GC population. This suggests that NSCs in faint dEs might have formed by different processes than the NSCs in brighter dEs. K. Fahrion et al. (2021, 2022a) studied star formation histories of 34 nucleated galaxies from the Fornax cluster and Local Volume using MUSE integral field unit spectra. They quantified the mass fraction of NSCs likely formed through in situ star formation by f_{insitu} and found a positive correlation with $\log M_{host}$, and concluded that the transition of dominant NSC formation channels occurs at roughly $\log M_{host} \sim 9$ (K. Fahrion et al. 2022b). N. Kacharov et al. (2018) also studied six galaxies with high-resolution optical spectra and found very young (<1 Gyr) stellar populations in their NSCs, suggesting prolonged in situ star formation. N. Neumayer et al. (2020) presented the relation between metallicities and mass of 35 NSCs and their host galaxies with spectroscopic metallicities available in the literature by then, and noticed an apparent transition at $\log M_{host} \sim 9$. The N. Neumayer et al. (2020) spectroscopic sample covers a galaxy mass range of $10^8\ M_\odot$ to $10^{9.7}\ M_\odot$.

The present work improves upon previous spectroscopic studies of NSCs and their host galaxies by increasing the sample size by more than a factor of three with consistent treatment of spectral extraction and stellar population modeling. Our sample covers a galaxy stellar mass range of $\log M_{host} \sim 6.5$ to $\log M_{host} \sim 11$.

We find the NSC metallicities have a stronger correlation with their host galaxy mass than NSC mass (Section 4.1; see also K. Fahrion et al. 2022a). This suggests that NSCs coevolve with their host galaxies. At $\log M_{host} > 8.5$, NSCs have

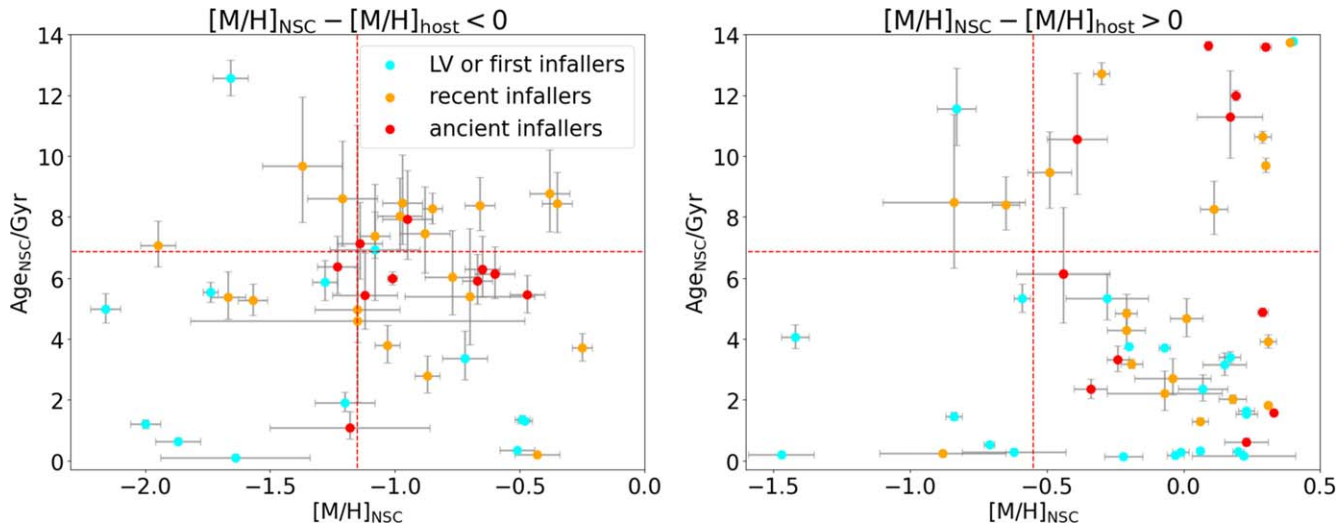

Figure 11. Similar to Figure 6, except that the sample is divided into subsamples according to the phase-space classification (see Figure 3 and Section 3.4), as indicated in the legend.

increasingly higher average metallicities than typical red GCs in their host, implying that the GC infall–merger channel becomes more and more insignificant in more massive galaxies, while at $\log M_{\rm host} < 8.5$, NSCs have average metallicities close to that of typical red GCs but systematically below the circum-NSC host. This suggests that NSCs in low-mass galaxies mainly formed through inspiral–merger of red GCs that formed prior to the formation of the bulk of their circum-NSC host stellar populations. Alternatively, NSCs and red GCs may simply be two families of star clusters that formed at a similar epoch but in different spatial locations (R. Sánchez-Janssen et al. 2019). In Section 5.2, we will demonstrate the efficacy of GC inspiral–merger in producing NSCs in low-mass galaxies.

The broad galaxy mass coverage of our sample enables the discovery of a broad peak of relative metal enrichment of NSCs with respect to the circum-NSC host regions near $\log M_{\rm host} \sim 9.8$, beyond which the average NSC–host metallicity difference $[{\rm M/H}]_{\rm diff}$ decreases with galaxy mass, reaching zero average difference near $\log M_{\rm host} \sim 11$. This indicates that in situ star formation of NSCs is currently most active in these galaxies.

The relatively large sample size also enables the discovery that a major group of NSCs with $[{\rm M/H}]_{\rm diff} > 0$ follow a negative age–metallicity correlation (Figure 6). This is vivid evidence for an extended period of metal enrichment of NSCs through in situ star formation. An early intensive formation followed by a quick quenching may explain the subdominant group of NSCs with old age and high metallicities in the subsample with $[{\rm M/H}]_{\rm diff} > 0$. No age–metallicity correlation is found for the subsample with $[{\rm M/H}]_{\rm diff} < 0$.

5.2. The Contribution of Dynamical-friction-driven GC Inspiral to NSC Formation

The finding that the NSC metallicity becomes systematically lower than (similar to) that of the circum-NSC host (typical red GCs) toward the lower galaxy mass end ($\log M_{\rm host} \lesssim 9.5$; Figures 4 and 5) is in line with the GC inspiral–merger scenario of NSC formation. Dynamical friction is the key process that drives the inspiral of GCs. In this section, we perform a test of the relevance of dynamical friction to the formation of NSCs with simplified models. By assuming a standard isothermal dark matter halo, the formula for the dynamical friction time of a GC (from an initial radius r_i to the center of the galaxy) is reduced to (J. Binney & S. Tremaine 1987)

$$t_{\rm DF} = \frac{2.64 \times 10^2}{\ln\Lambda}\left(\frac{r_i}{2\ {\rm kpc}}\right)^2\left(\frac{v_c}{250\ {\rm km\ s^{-1}}}\right)\left(\frac{10^6\,M_\odot}{M}\right){\rm Gyr}, \quad (4)$$

where v_c is the circular velocity of a GC with mass M at radius r_i of an isothermal galaxy halo. The Coulomb logarithm $\ln\Lambda$ is set to 10. With this formula, we determine whether or not a GC of given mass and initial galactocentric radius can spiral into the centers of galaxies in 10 Gyr. To set up the initial spatial distribution of GCs in galaxies of different mass, we adopt various observational scaling relations of galaxies available in the recent literature (see below), which allows us to evaluate the total number and mass of GCs that would spiral to the center of a galaxy and contribute to the assembly of NSCs. The predicted relation between NSC mass and galaxy mass can be compared to observations.

To construct the empirical model, we assume the host galaxies obey the observed effective radial size–mass relation (L. Mowla et al. 2019), the Sérsic index–galaxy stellar mass relation (A. W. Graham et al. 2006, Equation (12)), and the galaxy halo–stellar mass relation (A. Rodríguez-Puebla et al. 2017, Equation (66)). The total mass of the GC system of a galaxy is estimated based on its linear correlation with galaxy halo mass (W. E. Harris et al. 2017). In addition, the GC system is assumed to follow a Gaussian mass function, with a mean of $10^{5.3}\ M_\odot$ and logarithmic standard deviation of 0.5 (A. Jordán et al. 2007). To estimate the number of red GCs and blue GCs, we adopt the positive relation between the fraction of red GCs and galaxy stellar mass found by E. W. Peng et al. (2006). To set up the spatial distribution of blue and red GCs, we adopt the recently observed effective radius–galaxy halo mass relations for blue and red GC systems (S. Lim et al. 2024, Equations (17) and (18)), and further assume the GC systems follow Sérsic radial profiles with the same Sérsic indices as galaxy starlight.

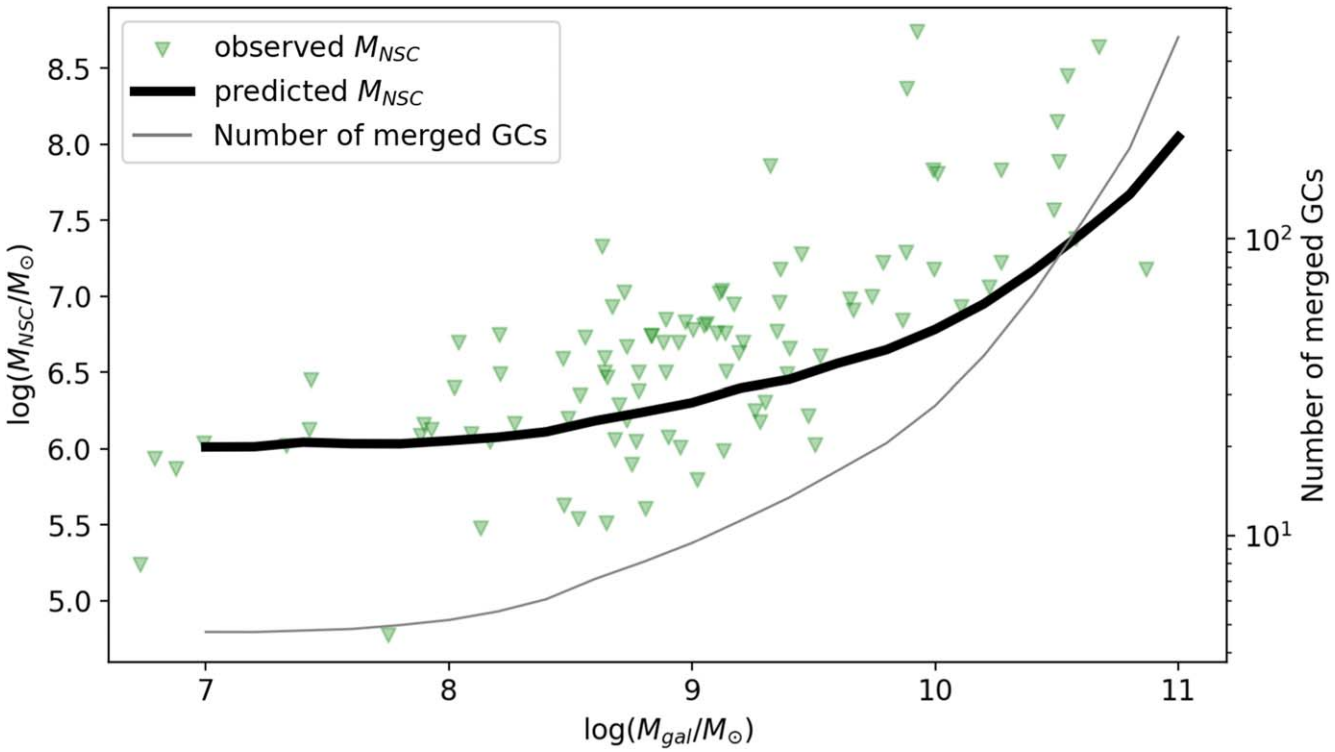

Figure 12. Comparison of the observed and predicted relations between NSC mass and galaxy stellar mass. The green inverted triangles represent the observed sample studied in this work. The black (gray) curve is the relation between the average NSC mass (number of merged GCs) and the galaxy mass predicted by a model of NSC formation through dynamical-friction-driven inspiral and merger. See Section 5.2 for details.

With the above model setting, we estimate the number and mass of GCs that would spiral into the center of the host (and thus contribute to the predicted NSC mass) in 10 Gyr for a series of input galaxy stellar masses ranging from 10^7 to 10^{11} $M_\odot$. A Monte Carlo method is adopted to randomly draw GCs (1000 times) according to the Gaussian GC mass function for given total GC mass and galactocentric radius. The predicted relations between NSC mass and number of GCs and galaxy stellar mass are shown in Figure 12. The predicted average $M_{\rm NSC}$ increases steadily with galaxy stellar mass, and the slope of the relation gradually steepens at higher galaxy mass. In addition, the average number of merged GCs also increases with galaxy mass. Note that the estimation based on existing GCs may be literally regarded as the future growth potential of NSCs through dynamical friction. However, considering that dynamical-friction-driven migration has been a continuous process, the growth potential also reflects the past growth efficiency driven by inspiral of classical GCs.

The predicted relation between NSC mass and galaxy stellar mass is in remarkable agreement with the average trend of the observed sample at $\log M_{\rm host} < 9.5$, which is in line with the prevalent notion in the literature. At higher galaxy mass, the observed NSC masses are systematically higher than predictions. The agreement at low galaxy masses reinforces the notion that GC inspiral–merger is the dominant NSC formation mechanism in these galaxies.

The relatively low predicted $M_{\rm NSC}$ at $\log M_{\rm gal} > 9.5$ may suggest that NSC formation mechanisms other than GC inspiral play important roles in these galaxies. The systematic discrepancy may be also partly attributed to ignoring the history of galaxy growth in our simple model. The present-day high-mass galaxies may have experienced more significant and active growth (via in situ star formation, accretion, or galaxy mergers) than lower-mass galaxies, and the overall inspiral efficiency of GCs in the high-mass galaxies could be higher at an earlier epoch than that predicted by our model. Nevertheless, it is noteworthy that $\log M_{\rm host} \sim 9.5$ is also where we find systematically higher $[{\rm M/H}]_{\rm NSC}$ than $[{\rm M/H}]_{\rm host}$ (e.g., Figure 5) toward higher galaxy mass, which implies an important role for in situ star formation in the NSC formation of these relatively high-mass galaxies.

The NSC formation scenario of dynamical-friction-driven cluster inspiral has been explored with theoretical models in the literature. However, most previous studies focused on exploring the possible parameter space—such as the mass function and spatial distribution of star clusters and the structural properties of galaxies—that can explain the observed NSCs within the framework of the dynamical friction scenario (e.g., K. Bekki 2010; M. Arca-Sedda & R. Capuzzo-Dolcetta 2014; R. Leaman & G. van de Ven 2022). Our analysis differs from previous studies by performing an explicit test of dynamical friction of classical GCs, based exclusively on observed scaling relations established in the recent literature for GCs and galaxy structures, with virtually no free parameter. Such a simple and clean test is worthwhile, especially given the theoretical uncertainties such as the formation of star clusters, disruption efficiencies, and the contribution of in situ star formation to NSCs.

According to previous studies (e.g., M. Arca-Sedda & R. Capuzzo-Dolcetta 2014), the effect of cluster disruption is expected to be significant only in relatively massive galaxies. Therefore, the deviation of the predicted NSC mass from the observed ones in high-mass galaxies would be even more significant if the effect of cluster disruption were included. In addition, our analysis ignores the plausible effect of NSC erosion caused by massive black hole binaries located near the

center of relatively massive galaxies (e.g., F. Antonini et al. 2015), which would further reduce the NSC mass predicted by our models toward the high-mass end. Lastly, we point out that any star clusters (being young or old, gas-rich or gas-poor) that are massive enough and survive long enough may be driven to the center of the galaxy through dynamical friction. Therefore, our empirical model is far from being flawless, and there is no doubt that more sophisticated models involving both formation and disruption histories of star clusters within a framework of hierarchical and continuous galaxy assembly is the way toward a complete understanding of NSC formation.

6. Conclusions

To shed light on the formation mechanisms of nuclear star clusters, we collect VLT optical spectroscopic observations of nuclear regions of 97 galaxies in the Local Group, Virgo cluster, and Fornax cluster. Among the sample, 29 are first analyzed in this work. We perform uniform data processing, subtract underlying host galaxy spectra from NSCs, and derive the stellar population properties (mean age, mean metallicity, $[\alpha/\mathrm{Fe}]$) of both NSCs and the circum-NSC host regions. We explore the formation and growth mechanism of NSCs by analyzing the mass–metallicity distribution, NSC–host metallicity difference $[\mathrm{M/H}]_{\mathrm{diff}}$, age–metallicity relations, and the environmental dependence of the stellar population of NSCs. Our main results are summarized as follows.

(i) The NSC metallicities have a more significant correlation with their host galaxy mass than the NSC mass, suggesting that NSCs coevolve with their host galaxies. At $\log M_{\mathrm{host}} \gtrsim 8.5$, NSCs have increasingly higher average metallicities than typical red GCs toward the higher galaxy mass end, indicating that NSC formation mechanisms other than inspiral–merger of classical GCs become increasingly important toward higher galaxy mass. At $\log M_{\mathrm{host}} \lesssim 8.5$, NSCs have average metallicities similar to or slightly lower (toward the lower galaxy mass end) than those of red GCs, implying that GC inspiral–merger is the dominant formation channel of NSCs. Typical NSCs in the lowest-mass galaxies may have been formed even prior to the formation of most GCs.

(ii) We identify three galaxy mass regimes in the $[\mathrm{M/H}]_{\mathrm{diff}}$–galaxy stellar mass diagram. The three regimes are separated by $\log M_{\mathrm{host}}$ of 8.5 and 9.5 respectively. In the low-galaxy-mass regime (i.e., $\log M_{\mathrm{host}} \lesssim 8.5$), nearly all NSCs have lower metallicities than the circum-NSC host regions, while in the high-mass regime ($\log M_{\mathrm{host}} \gtrsim 9.5$), nearly all NSCs have higher metallicities than the circum-NSC host regions. In the intermediate-mass regime ($8.5 \lesssim \log M_{\mathrm{host}} \lesssim 9.5$), the fraction of NSCs with higher metallicities than the circum-NSC host is comparable to the fraction with lower metallicities. These findings suggest that NSC growth is sustained by continuous metal-enriched gas inflow from larger galactocentric distances in high-mass galaxies, while in low-mass galaxies enriched gas inflow to the NSC region has been largely suppressed with respect to the circum-host regions. In the intermediate-mass regime, larger $[\mathrm{M/H}]_{\mathrm{diff}}$ is primarily due to higher NSC metallicities rather than lower circum-host metallicities. The growth of NSCs through enriched gas inflow in intermediate-mass galaxies is probably sporadic in time, which results in a lack of correlation between $[\mathrm{M/H}]_{\mathrm{diff}}$ and NSC mass.

(iii) In the intermediate- and high-galaxy-mass regimes, the average $[\mathrm{M/H}]_{\mathrm{diff}}$ reaches a broad maximum at $\log M_{\mathrm{host}} \sim 9.8$, and drops toward both higher and lower galaxy masses. Galaxies with the highest $[\mathrm{M/H}]_{\mathrm{diff}}$ (i.e., >0.5) are mostly characterized by relatively low circum-NSC metallicities (instead of systematically high NSC metallicities), young NSC ages, and low NSC mass, suggesting that NSCs in these galaxies are at a relatively early stage of assembly through in situ star formation. Growth of NSCs toward higher galaxy masses is probably subjected to a significant negative influence through either tidal disruption of supermassive black holes or quenching by active galactic nuclei.

(iv) By dividing NSCs into subsamples with $[\mathrm{M/H}]_{\mathrm{diff}} < 0$ or >0, we find that the subsample of NSCs with $[\mathrm{M/H}]_{\mathrm{diff}} < 0$ have virtually no relation between light-weighted age and metallicity, while for the majority of NSCs in the subsample with $[\mathrm{M/H}]_{\mathrm{diff}} > 0$ there exists a negative age–metallicity correlation, irrespective of galaxy stellar mass, in line with an extended chemical enrichment history. A synchrony between the metal enrichment history of NSCs and the circum-NSC host for the subsample with $[\mathrm{M/H}]_{\mathrm{diff}} > 0$ is also reflected in a relatively high fraction of NSCs with similar $[\alpha/\mathrm{Fe}]$ to the circum-NSC host.

(v) A simplified empirical model of NSC formation through dynamical-friction-driven inspiral–merger of GCs based exclusively on various observed scaling relations of present-day galaxies explains the average relation between NSC mass and galaxy mass at $\log M_{\mathrm{host}} < 9.5$, in agreement with similar studies in the literature, implying that other formation mechanisms are inconsequential to NSC formation in dwarf galaxies. We find that about 10 or so GCs are sufficient to double the NSC mass in these low-mass galaxies. The empirical model fails to explain M_{NSC} at $\log M_{\mathrm{gal}} > 9.5$, which coincides with the "transition" mass where NSC metallicities are systematically higher than in the circum-NSC host, reinforcing that in situ star formation plays an important role in the assembly of NSCs of high-mass galaxies.

With the limited sample size in mind, we find no significant environmental dependence of the stellar population properties of NSCs, and no significant dependence on the Hubble type of host galaxies. Our homogeneous analysis of the stellar population properties of nearby NSCs reinforce the notion of a strong dependence of the assembly of NSCs on galaxy mass, with a seemingly abrupt transition near $\log M_{\mathrm{host}} \sim 9.0 \pm 0.5$.

Acknowledgments

We thank the anonymous referee for helpful suggestions that improved our manuscript. We acknowledge support from the NSFC (grant Nos. 12122303, 11973039, 11421303, 11973038, and 12233008). This work is also supported by the National Key Research and Development Program of China (grant No. 2023YFA1608100) and the China Manned Space Project (grant Nos. CMS-CSST-2021-B02 and CMS-CSST-2021-A07). We acknowledge support from the CAS Pioneer Hundred Talents Program, the Strategic Priority Research Program of Chinese Academy of Sciences (grant No. XDB

41000000), and the Cyrus Chun Ying Tang Foundations. We also acknowledge support from the Mid-career Researcher Program (grant No. RS-2023-00208957).

Appendix A
S/N of Spectra

The spectral S/Ns of NSCs and circum-host regions of our sample galaxies are given in Table 2.

Table 2
S/N of Spectra at 5000 Å

Galaxy	S/N_{NSC}	S/N_{host}	Instrument
NGC 247	112.76	24.57	X-Shooter
NGC 2784	74.43	123.83	X-Shooter
NGC 300	19.55	21.07	X-Shooter
NGC 3115	171.63	201.35	X-Shooter
NGC 3621	42.29	132.6	X-Shooter
NGC 5068	53.38	38.59	X-Shooter
NGC 5102	133.5	114.29	X-Shooter
NGC 5206	79.46	68.79	X-Shooter
NGC 5236	44.81	60.72	X-Shooter
NGC 628	53.15	40.6	X-Shooter
NGC 7713	26.45	17.83	X-Shooter
NGC 7793	108.89	26.61	X-Shooter
VCC 0216	11.91	14.58	FORS2
VCC 0308	7.09	18.7	FORS2
VCC 0389	8.12	13.15	FORS2
VCC 0490	10.49	13.53	FORS2
VCC 0545	11.72	10.83	FORS2
VCC 0592	6.09	12.72	FORS2
VCC 0725	9.17	6.45	FORS2
VCC 0765	8.05	15.98	FORS2
VCC 0786	2.77	5.61	MUSE
VCC 0856	9.69	11.65	FORS2
VCC 0871	3.9	11.29	FORS2
VCC 0916	7.47	8.85	FORS2
VCC 0929	9.4	12.91	FORS2
VCC 0940	8.57	10.48	FORS2
VCC 0965	10.93	11.24	FORS2
VCC 0990	5.68	16.13	FORS2
VCC 1069	5.11	10.42	FORS2
VCC 1073	1.9	12.45	FORS2
VCC 1104	3.96	8.67	FORS2
VCC 1122	5.46	8.17	FORS2
VCC 1167	16.19	10.0	FORS2
VCC 1185	7.3	9.61	FORS2
VCC 1254	12.96	8.25	FORS2
VCC 1261	11.18	17.35	FORS2
VCC 1304	4.94	9.5	FORS2
VCC 1308	6.59	15.36	FORS2
VCC 1333	16.46	3.95	FORS2
VCC 1348	19.65	9.64	FORS2
VCC 1353	10.43	12.48	FORS2
VCC 1355	8.6	11.37	FORS2
VCC 1386	2.89	14.54	FORS2
VCC 1389	11.25	10.46	FORS2
VCC 1407	11.31	17.94	FORS2
VCC 1431	9.08	12.47	FORS2
VCC 1491	2.8	1.99	FORS2
VCC 1661	14.07	7.18	FORS2
VCC 1826	6.61	15.19	FORS2
VCC 1861	10.02	11.79	FORS2
VCC 1945	7.98	9.73	FORS2
VCC 2019	8.21	14.22	FORS2
Circinus	0.38	0.21	MUSE
ESO 59-01	26.64	12.28	MUSE
FCC 119	10.07	18.9	MUSE
FCC 148	15.11	17.38	MUSE
FCC 153	12.66	14.87	MUSE
FCC 170	22.26	22.71	MUSE
FCC 177	13.79	15.48	MUSE
FCC 182	11.82	17.35	MUSE
FCC 188	18.49	6.9	MUSE
FCC 190	14.04	19.42	MUSE
FCC 193	14.8	23.92	MUSE
FCC 202	15.56	19.26	MUSE
FCC 207	11.93	9.36	MUSE
FCC 211	12.56	13.45	MUSE
FCC 215	13.66	3.24	MUSE
FCC 222	11.06	16.29	MUSE
FCC 223	13.91	7.2	MUSE
FCC 227	0.19	1.6	MUSE
FCC 245	0.11	2.3	MUSE
FCC 249	19.14	25.89	MUSE
FCC 255	11.86	18.49	MUSE
FCC 277	14.85	25.57	MUSE
FCC 301	13.17	21.41	MUSE
FCC 306	7.05	19.48	MUSE
FCC 310	11.2	20.13	MUSE
FCC 47	22.54	23.57	MUSE
FCC B1241	1.45	3.18	MUSE
IC 1959	35.00	30.21	MUSE
IC 5332	11.78	17.98	MUSE
KK 197	7.34	6.39	MUSE
KKS 58	13.81	5.82	MUSE
NGC 1487	20.59	40.92	MUSE
NGC 1705	17.14	2.64	MUSE
NGC 1796	3.97	11.75	MUSE
NGC 2835	17.71	15.39	MUSE
NGC 3274	2.93	0.62	MUSE
NGC 3368	13.89	18.05	MUSE
NGC 3489	16.17	15.19	MUSE
NGC 3593	2.52	13.4	MUSE
NGC 4592	11.04	25.22	MUSE
NGC 5253	0.26	0.1	MUSE
NGC 853	10.94	1.84	MUSE
UGC 3755	0.21	0.15	MUSE
UGC 5889	11.95	14.09	MUSE
UGC 8041	21.24	12.13	MUSE

Note. S/N_{NSC} and S/N_{host} are the signal-to-noise ratios of the spectra of NSCs and host galaxies before being smoothed to FORS2 resolution while the column "instrument" lists the instruments used to observe the spectra.

Appendix B
Light-weighted Stellar Population Properties of NSCs and Circum-NSC Host of Our Sample Galaxies

Light-weighted age and light-weighted metallicity as well as [α/Fe] of NSCs and circum-NSC host regions are given in Table 3 with their 1σ error.

Table 3
Stellar Population Properties of NSC and Circum-NSC Host Regions

Galaxy	$\mathrm{Age_{NSC}}$ (Gyr)	$[\mathrm{M/H}]_{\mathrm{NSC}}$	$[\alpha/\mathrm{Fe}]_{\mathrm{NSC}}$	$\mathrm{Age_{host}}$ (Gyr)	$[\mathrm{M/H}]_{\mathrm{host}}$	$[\alpha/\mathrm{Fe}]_{\mathrm{host}}$
NGC 247	$0.53^{+0.03}_{-0.03}$	$-0.71^{+0.02}_{-0.02}$	$-0.16^{+0.08}_{-0.08}$	$2.74^{+0.16}_{-0.15}$	$-1.02^{+0.03}_{-0.03}$	$1.13^{+0.14}_{-0.14}$
NGC 2784	$13.77^{+0.02}_{-0.02}$	$0.4^{+0.0}_{-0.0}$	$0.22^{+0.02}_{-0.02}$	$11.06^{+0.1}_{-0.1}$	$0.39^{+0.01}_{-0.01}$	$0.36^{+0.01}_{-0.01}$
NGC 300	$1.46^{+0.13}_{-0.12}$	$-0.84^{+0.03}_{-0.03}$	$0.42^{+0.13}_{-0.13}$	$5.92^{+0.55}_{-0.51}$	$-1.56^{+0.04}_{-0.04}$	$0.63^{+0.1}_{-0.1}$
NGC 3115	$13.78^{+0.02}_{-0.02}$	$0.4^{+0.0}_{-0.0}$	$0.45^{+0.01}_{-0.01}$	$12.14^{+0.03}_{-0.03}$	$0.4^{+0.0}_{-0.0}$	$0.31^{+0.0}_{-0.0}$
NGC 3621	$1.64^{+0.09}_{-0.08}$	$0.23^{+0.03}_{-0.03}$	$-0.01^{+0.06}_{-0.06}$	$1.7^{+0.08}_{-0.08}$	$-0.6^{+0.03}_{-0.03}$	$0.17^{+0.03}_{-0.03}$
NGC 5068	$0.29^{+0.02}_{-0.02}$	$-0.01^{+0.03}_{-0.03}$	$0.4^{+0.1}_{-0.1}$	$1.15^{+0.15}_{-0.14}$	$-0.83^{+0.05}_{-0.05}$	$-0.12^{+0.06}_{-0.06}$
NGC 5102	$0.32^{+0.0}_{-0.0}$	$0.06^{+0.01}_{-0.01}$	$0.16^{+0.06}_{-0.06}$	$0.92^{+0.04}_{-0.04}$	$-0.29^{+0.01}_{-0.01}$	$-0.04^{+0.01}_{-0.01}$
NGC 5206	$3.76^{+0.07}_{-0.07}$	$-0.2^{+0.01}_{-0.01}$	$0.02^{+0.02}_{-0.02}$	$2.96^{+0.13}_{-0.13}$	$-0.2^{+0.01}_{-0.01}$	$-0.06^{+0.02}_{-0.02}$
NGC 5236	$1.32^{+0.07}_{-0.07}$	$-0.48^{+0.03}_{-0.03}$	$0.8^{+0.02}_{-0.02}$	$0.73^{+0.03}_{-0.03}$	$-0.05^{+0.03}_{-0.03}$	$0.62^{+0.03}_{-0.03}$
NGC 628	$3.72^{+0.09}_{-0.09}$	$-0.07^{+0.02}_{-0.02}$	$0.26^{+0.08}_{-0.08}$	$6.5^{+0.77}_{-0.69}$	$-0.5^{+0.05}_{-0.05}$	$-0.09^{+0.01}_{-0.01}$
NGC 7713	$0.19^{+0.01}_{-0.01}$	$-0.03^{+0.03}_{-0.03}$	$0.17^{+0.05}_{-0.05}$	$2.83^{+0.21}_{-0.19}$	$-0.95^{+0.04}_{-0.04}$	$0.08^{+0.07}_{-0.07}$
NGC 7793	$0.3^{+0.01}_{-0.01}$	$0.2^{+0.02}_{-0.02}$	$0.07^{+0.03}_{-0.03}$	$1.66^{+0.11}_{-0.11}$	$-1.04^{+0.04}_{-0.04}$	$0.07^{+0.04}_{-0.04}$
VCC 0216	$2.78^{+0.67}_{-0.54}$	$-0.87^{+0.05}_{-0.05}$	$-0.08^{+0.03}_{-0.03}$	$4.18^{+0.72}_{-0.61}$	$-0.49^{+0.07}_{-0.07}$	$0.78^{+0.05}_{-0.05}$
VCC 0308	$2.36^{+0.48}_{-0.4}$	$0.07^{+0.09}_{-0.09}$	$0.29^{+0.05}_{-0.05}$	$2.61^{+0.52}_{-0.43}$	$-0.16^{+0.07}_{-0.07}$	$-0.08^{+0.04}_{-0.04}$
VCC 0389	$2.22^{+0.73}_{-0.55}$	$-0.07^{+0.21}_{-0.21}$	$-0.09^{+0.02}_{-0.02}$	$7.64^{+0.8}_{-0.73}$	$-0.26^{+0.05}_{-0.05}$	$-0.01^{+0.02}_{-0.02}$
VCC 0490	$8.43^{+1.04}_{-0.93}$	$-0.35^{+0.06}_{-0.06}$	$-0.28^{+0.01}_{-0.01}$	$6.1^{+0.61}_{-0.55}$	$-0.26^{+0.04}_{-0.04}$	$0.23^{+0.04}_{-0.04}$
VCC 0545	$8.4^{+0.93}_{-0.83}$	$-0.65^{+0.05}_{-0.05}$	$0.49^{+0.05}_{-0.05}$	$10.12^{+1.09}_{-0.98}$	$-0.72^{+0.05}_{-0.05}$	$0.16^{+0.08}_{-0.08}$
VCC 0592	$9.68^{+2.28}_{-1.85}$	$-1.37^{+0.16}_{-0.16}$	$0.15^{+0.01}_{-0.01}$	$3.65^{+0.72}_{-0.6}$	$-0.48^{+0.1}_{-0.1}$	$0.38^{+0.0}_{-0.0}$
VCC 0725	$6.03^{+1.53}_{-1.22}$	$-0.77^{+0.11}_{-0.11}$	…	$9.52^{+1.59}_{-1.36}$	$-0.72^{+0.08}_{-0.08}$	…
VCC 0765	$8.76^{+1.44}_{-1.24}$	$-0.38^{+0.08}_{-0.08}$	$0.75^{+0.02}_{-0.02}$	$4.8^{+1.09}_{-0.89}$	$-0.11^{+0.12}_{-0.12}$	$-0.0^{+0.0}_{-0.0}$
VCC 0786	$8.6^{+1.89}_{-1.55}$	$-1.21^{+0.14}_{-0.14}$	…	$7.55^{+1.66}_{-1.36}$	$-0.49^{+0.13}_{-0.13}$	…
VCC 0856	$4.67^{+0.66}_{-0.58}$	$0.01^{+0.06}_{-0.06}$	$-0.09^{+0.01}_{-0.01}$	$10.13^{+0.87}_{-0.81}$	$-0.66^{+0.04}_{-0.04}$	$0.12^{+0.03}_{-0.03}$
VCC 0871	$1.08^{+0.54}_{-0.36}$	$-1.18^{+0.32}_{-0.32}$	$0.61^{+0.05}_{-0.05}$	$6.52^{+1.55}_{-1.26}$	$-0.52^{+0.1}_{-0.1}$	$-0.12^{+0.0}_{-0.0}$
VCC 0916	$13.6^{+0.12}_{-0.12}$	$0.3^{+0.02}_{-0.02}$	$-0.03^{+0.0}_{-0.0}$	$10.12^{+0.72}_{-0.67}$	$0.16^{+0.05}_{-0.05}$	$0.18^{+0.0}_{-0.0}$
VCC 0929	$8.26^{+0.92}_{-0.83}$	$0.11^{+0.05}_{-0.05}$	$0.22^{+0.02}_{-0.02}$	$10.37^{+0.96}_{-0.88}$	$-0.16^{+0.04}_{-0.04}$	$0.74^{+0.01}_{-0.01}$
VCC 0940	$5.45^{+0.65}_{-0.58}$	$-0.47^{+0.07}_{-0.07}$	$-0.18^{+0.01}_{-0.01}$	$7.56^{+0.62}_{-0.57}$	$-0.43^{+0.04}_{-0.04}$	$0.18^{+0.0}_{-0.0}$
VCC 0965	$2.35^{+0.34}_{-0.3}$	$-0.34^{+0.06}_{-0.06}$	$-0.37^{+0.02}_{-0.02}$	$4.31^{+0.48}_{-0.43}$	$-0.47^{+0.05}_{-0.05}$	$-0.21^{+0.0}_{-0.0}$
VCC 0990	$4.29^{+0.7}_{-0.6}$	$-0.21^{+0.07}_{-0.07}$	$-0.08^{+0.03}_{-0.03}$	$7.1^{+0.44}_{-0.41}$	$-0.49^{+0.03}_{-0.03}$	$-0.08^{+0.01}_{-0.01}$
VCC 1069	$4.96^{+1.37}_{-1.07}$	$-1.15^{+0.17}_{-0.17}$	$0.21^{+0.03}_{-0.03}$	$8.74^{+0.85}_{-0.78}$	$-0.88^{+0.05}_{-0.05}$	$-0.23^{+0.0}_{-0.0}$
VCC 1073	$11.29^{+1.53}_{-1.35}$	$0.17^{+0.12}_{-0.12}$	$0.67^{+0.0}_{-0.0}$	$12.71^{+0.7}_{-0.67}$	$-0.13^{+0.04}_{-0.04}$	$0.1^{+0.0}_{-0.0}$
VCC 1104	$7.93^{+1.6}_{-1.33}$	$-0.95^{+0.1}_{-0.1}$	$0.1^{+0.03}_{-0.03}$	$5.34^{+0.66}_{-0.59}$	$-0.6^{+0.07}_{-0.07}$	$-0.11^{+0.0}_{-0.0}$
VCC 1122	$2.7^{+0.66}_{-0.53}$	$-0.04^{+0.14}_{-0.14}$	$-0.02^{+0.0}_{-0.0}$	$10.64^{+1.4}_{-1.24}$	$-0.37^{+0.07}_{-0.07}$	$0.15^{+0.01}_{-0.01}$
VCC 1167	$8.02^{+1.25}_{-1.08}$	$-0.98^{+0.09}_{-0.09}$	$0.25^{+0.08}_{-0.08}$	$10.44^{+1.14}_{-1.02}$	$-0.55^{+0.06}_{-0.06}$	$0.05^{+0.04}_{-0.04}$
VCC 1185	$5.44^{+1.38}_{-1.1}$	$-1.12^{+0.13}_{-0.13}$	$-0.3^{+0.14}_{-0.14}$	$11.42^{+0.74}_{-0.7}$	$-0.45^{+0.03}_{-0.03}$	$-0.22^{+0.09}_{-0.09}$
VCC 1254	$3.71^{+0.48}_{-0.43}$	$-0.25^{+0.04}_{-0.04}$	$0.12^{+0.01}_{-0.01}$	$6.7^{+0.82}_{-0.73}$	$-0.06^{+0.07}_{-0.07}$	$0.24^{+0.03}_{-0.03}$
VCC 1261	$2.02^{+0.15}_{-0.14}$	$0.18^{+0.05}_{-0.05}$	$-0.51^{+0.14}_{-0.14}$	$4.11^{+0.42}_{-0.38}$	$-0.34^{+0.03}_{-0.03}$	$0.11^{+0.01}_{-0.01}$
VCC 1304	$6.92^{+2.15}_{-1.64}$	$-1.08^{+0.18}_{-0.18}$	$0.35^{+0.09}_{-0.09}$	$5.53^{+0.92}_{-0.79}$	$-0.48^{+0.05}_{-0.05}$	$-0.27^{+0.01}_{-0.01}$
VCC 1308	$3.33^{+0.44}_{-0.39}$	$-0.24^{+0.04}_{-0.04}$	$0.41^{+0.04}_{-0.04}$	$6.32^{+0.43}_{-0.4}$	$-0.53^{+0.04}_{-0.04}$	$-0.07^{+0.02}_{-0.02}$
VCC 1333	$7.37^{+0.8}_{-0.72}$	$-1.08^{+0.06}_{-0.06}$	$0.37^{+0.04}_{-0.04}$	$7.03^{+3.65}_{-2.4}$	$-1.03^{+0.24}_{-0.24}$	$0.78^{+1.78}_{-1.78}$
VCC 1348	$5.91^{+0.87}_{-0.76}$	$-0.67^{+0.06}_{-0.06}$	$0.2^{+0.02}_{-0.02}$	$11.74^{+1.15}_{-1.05}$	$-0.41^{+0.05}_{-0.05}$	$0.35^{+0.02}_{-0.02}$
VCC 1353	$3.37^{+0.89}_{-0.71}$	$-0.72^{+0.09}_{-0.09}$	$-0.08^{+0.03}_{-0.03}$	$2.55^{+0.58}_{-0.47}$	$-0.41^{+0.09}_{-0.09}$	$0.49^{+0.04}_{-0.04}$
VCC 1355	$6.29^{+1.07}_{-0.91}$	$-0.65^{+0.07}_{-0.07}$	$-0.23^{+0.03}_{-0.03}$	$5.35^{+1.8}_{-1.34}$	$-0.26^{+0.14}_{-0.14}$	$-0.01^{+0.05}_{-0.05}$
VCC 1386	$10.55^{+2.19}_{-1.81}$	$-0.39^{+0.11}_{-0.11}$	…	$10.05^{+1.01}_{-0.92}$	$-0.69^{+0.04}_{-0.04}$	…
VCC 1389	$7.12^{+1.36}_{-1.14}$	$-1.14^{+0.09}_{-0.09}$	$0.13^{+0.11}_{-0.11}$	$7.63^{+0.94}_{-0.84}$	$-0.86^{+0.06}_{-0.06}$	$-0.09^{+0.02}_{-0.02}$
VCC 1407	$6.37^{+1.01}_{-0.87}$	$-1.23^{+0.08}_{-0.08}$	$0.12^{+0.09}_{-0.09}$	$9.91^{+0.57}_{-0.54}$	$-0.6^{+0.03}_{-0.03}$	$0.14^{+0.02}_{-0.02}$
VCC 1431	$6.13^{+0.9}_{-0.79}$	$-0.6^{+0.08}_{-0.08}$	$0.59^{+0.01}_{-0.01}$	$11.05^{+0.98}_{-0.9}$	$-0.4^{+0.03}_{-0.03}$	$0.42^{+0.0}_{-0.0}$
VCC 1491	$6.14^{+2.17}_{-1.6}$	$-0.44^{+0.17}_{-0.17}$	$0.56^{+0.02}_{-0.02}$	$6.03^{+2.94}_{-1.98}$	$-0.59^{+0.31}_{-0.31}$	$-0.43^{+0.03}_{-0.03}$
VCC 1661	$8.45^{+1.6}_{-1.34}$	$-0.97^{+0.08}_{-0.08}$	$-0.04^{+0.02}_{-0.02}$	$6.59^{+1.65}_{-1.32}$	$-0.3^{+0.12}_{-0.12}$	$-0.07^{+0.02}_{-0.02}$
VCC 1826	$9.47^{+1.33}_{-1.17}$	$-0.49^{+0.08}_{-0.08}$	$-0.27^{+0.06}_{-0.06}$	$9.03^{+0.82}_{-0.75}$	$-0.62^{+0.05}_{-0.05}$	$-0.19^{+0.02}_{-0.02}$
VCC 1861	$8.38^{+0.92}_{-0.83}$	$-0.66^{+0.06}_{-0.06}$	$-0.2^{+0.02}_{-0.02}$	$7.25^{+0.53}_{-0.49}$	$-0.08^{+0.03}_{-0.03}$	$0.03^{+0.02}_{-0.02}$
VCC 1945	$7.45^{+1.54}_{-1.28}$	$-0.88^{+0.1}_{-0.1}$	$0.63^{+0.14}_{-0.14}$	$6.41^{+1.41}_{-1.15}$	$-0.52^{+0.13}_{-0.13}$	$-0.04^{+0.01}_{-0.01}$
VCC 2019	$4.85^{+0.63}_{-0.56}$	$-0.21^{+0.04}_{-0.04}$	$-0.16^{+0.02}_{-0.02}$	$8.46^{+1.3}_{-1.13}$	$-0.55^{+0.06}_{-0.06}$	$-0.18^{+0.02}_{-0.02}$
Circinus	$0.16^{+0.04}_{-0.03}$	$0.22^{+0.19}_{-0.19}$	$0.60^{+0.12}_{-0.12}$	$0.26^{+0.02}_{-0.02}$	$0.12^{+0.16}_{-0.16}$	$0.65^{+0.04}_{-0.04}$
ESO 59-01	$5.54^{+0.34}_{-0.32}$	$-1.74^{+0.03}_{-0.03}$	$0.16^{+0.08}_{-0.08}$	$8.92^{+1.02}_{-0.92}$	$-1.68^{+0.06}_{-0.06}$	$0.36^{+0.07}_{-0.07}$
FCC 119	$0.2^{+0.03}_{-0.03}$	$-0.43^{+0.09}_{-0.09}$	$-0.22^{+0.49}_{-0.49}$	$2.05^{+0.17}_{-0.16}$	$-0.42^{+0.02}_{-0.02}$	$-0.06^{+0.02}_{-0.02}$
FCC 148	$1.83^{+0.07}_{-0.07}$	$0.31^{+0.01}_{-0.01}$	$-0.1^{+0.03}_{-0.03}$	$2.52^{+0.16}_{-0.15}$	$-0.05^{+0.01}_{-0.01}$	$0.06^{+0.08}_{-0.08}$
FCC 153	$3.92^{+0.22}_{-0.21}$	$0.31^{+0.03}_{-0.03}$	$-0.07^{+0.04}_{-0.04}$	$4.36^{+0.17}_{-0.17}$	$0.2^{+0.02}_{-0.02}$	$0.08^{+0.01}_{-0.01}$

Table 3
(Continued)

Galaxy	$\mathrm{Age_{NSC}}$ (Gyr)	$[\mathrm{M/H}]_{\mathrm{NSC}}$	$[\alpha/\mathrm{Fe}]_{\mathrm{NSC}}$	$\mathrm{Age_{host}}$ (Gyr)	$[\mathrm{M/H}]_{\mathrm{host}}$	$[\alpha/\mathrm{Fe}]_{\mathrm{host}}$
FCC 170	$12.0^{+0.17}_{-0.17}$	$0.19^{+0.02}_{-0.02}$	$0.2^{+0.02}_{-0.02}$	$12.93^{+0.31}_{-0.31}$	$-0.18^{+0.02}_{-0.02}$	$0.22^{+0.01}_{-0.01}$
FCC 177	$1.57^{+0.04}_{-0.04}$	$0.33^{+0.01}_{-0.01}$	$0.37^{+0.0}_{-0.0}$	$4.45^{+0.12}_{-0.12}$	$0.04^{+0.01}_{-0.01}$	$0.05^{+0.0}_{-0.0}$
FCC 182	$13.63^{+0.15}_{-0.15}$	$0.09^{+0.01}_{-0.01}$	$0.05^{+0.01}_{-0.01}$	$5.83^{+0.37}_{-0.35}$	$-0.29^{+0.02}_{-0.02}$	$0.11^{+0.01}_{-0.01}$
FCC 188	$5.99^{+0.21}_{-0.2}$	$-1.01^{+0.02}_{-0.02}$	$0.07^{+0.03}_{-0.03}$	$5.3^{+0.77}_{-0.67}$	$-0.83^{+0.09}_{-0.09}$	$0.23^{+0.1}_{-0.1}$
FCC 190	$4.88^{+0.15}_{-0.14}$	$0.29^{+0.02}_{-0.02}$	$-0.02^{+0.06}_{-0.06}$	$10.36^{+0.77}_{-0.72}$	$-0.26^{+0.03}_{-0.03}$	$0.14^{+0.01}_{-0.01}$
FCC 193	$13.74^{+0.02}_{-0.02}$	$0.39^{+0.0}_{-0.0}$	$0.13^{+0.02}_{-0.02}$	$10.08^{+0.28}_{-0.27}$	$-0.08^{+0.02}_{-0.02}$	$0.15^{+0.01}_{-0.01}$
FCC 202	$8.27^{+0.51}_{-0.48}$	$-0.85^{+0.04}_{-0.04}$	$-0.16^{+0.03}_{-0.03}$	$5.08^{+0.33}_{-0.31}$	$-0.35^{+0.03}_{-0.03}$	$0.14^{+0.0}_{-0.0}$
FCC 207	$0.61^{+0.15}_{-0.12}$	$0.23^{+0.08}_{-0.08}$	$0.01^{+3.77}_{-3.77}$	$10.61^{+1.33}_{-1.18}$	$-0.61^{+0.1}_{-0.1}$	$-0.14^{+0.02}_{-0.02}$
FCC 211	$3.79^{+0.67}_{-0.57}$	$-1.03^{+0.05}_{-0.05}$	$0.67^{+0.05}_{-0.05}$	$4.09^{+0.33}_{-0.3}$	$-0.81^{+0.04}_{-0.04}$	$-0.04^{+0.01}_{-0.01}$
FCC 215	$5.28^{+0.53}_{-0.49}$	$-1.57^{+0.06}_{-0.06}$	$0.57^{+0.05}_{-0.05}$	$1.41^{+0.31}_{-0.25}$	$-1.5^{+0.24}_{-0.24}$	$-0.23^{+2.06}_{-2.06}$
FCC 222	$5.37^{+0.82}_{-0.71}$	$-1.67^{+0.07}_{-0.07}$	$-0.29^{+0.53}_{-0.53}$	$7.5^{+0.59}_{-0.55}$	$-0.64^{+0.04}_{-0.04}$	$0.11^{+0.01}_{-0.01}$
FCC 223	$7.07^{+0.79}_{-0.71}$	$-1.95^{+0.07}_{-0.07}$	…	$9.9^{+1.33}_{-1.17}$	$-1.4^{+0.08}_{-0.08}$	…
FCC 227	$4.59^{+6.41}_{-2.67}$	$-1.15^{+0.67}_{-0.67}$	…	$1.55^{+1.93}_{-0.86}$	$-0.74^{+0.72}_{-0.72}$	…
FCC 245	$8.48^{+2.89}_{-2.15}$	$-0.84^{+0.26}_{-0.26}$	…	$10.06^{+1.85}_{-1.57}$	$-0.86^{+0.15}_{-0.15}$	…
FCC 249	$10.63^{+0.19}_{-0.19}$	$0.29^{+0.03}_{-0.03}$	$0.31^{+0.01}_{-0.01}$	$12.67^{+0.39}_{-0.37}$	$-0.47^{+0.02}_{-0.02}$	$0.37^{+0.01}_{-0.01}$
FCC 255	$1.3^{+0.11}_{-0.1}$	$0.06^{+0.03}_{-0.03}$	$-0.18^{+0.07}_{-0.07}$	$3.96^{+0.18}_{-0.17}$	$-0.27^{+0.01}_{-0.01}$	$0.09^{+0.01}_{-0.01}$
FCC 277	$3.18^{+0.16}_{-0.15}$	$-0.19^{+0.04}_{-0.04}$	$0.31^{+0.03}_{-0.03}$	$8.1^{+0.71}_{-0.65}$	$-0.78^{+0.03}_{-0.03}$	$0.67^{+0.01}_{-0.01}$
FCC 301	$3.4^{+0.19}_{-0.18}$	$0.17^{+0.04}_{-0.04}$	$-0.0^{+0.01}_{-0.01}$	$7.96^{+0.35}_{-0.34}$	$-0.72^{+0.03}_{-0.03}$	$0.16^{+0.01}_{-0.01}$
FCC 306	$0.25^{+0.05}_{-0.04}$	$-0.88^{+0.23}_{-0.23}$	$0.35^{+0.37}_{-0.37}$	$0.47^{+0.05}_{-0.04}$	$-0.99^{+0.05}_{-0.05}$	$0.1^{+0.07}_{-0.07}$
FCC 310	$9.7^{+0.24}_{-0.24}$	$0.3^{+0.01}_{-0.01}$	$0.0^{+0.01}_{-0.01}$	$6.26^{+0.2}_{-0.19}$	$-0.22^{+0.01}_{-0.01}$	$0.08^{+0.0}_{-0.0}$
FCC 47	$12.72^{+0.36}_{-0.35}$	$-0.3^{+0.03}_{-0.03}$	$0.46^{+0.01}_{-0.01}$	$10.77^{+0.4}_{-0.39}$	$-0.67^{+0.02}_{-0.02}$	$0.31^{+0.05}_{-0.05}$
FCCB 1237	$5.39^{+2.22}_{-1.57}$	$-0.7^{+0.26}_{-0.26}$	…	$10.39^{+1.63}_{-1.41}$	$-0.12^{+0.11}_{-0.11}$	…
IC 1959	$11.55^{+1.34}_{-1.2}$	$-0.83^{+0.07}_{-0.07}$	$-0.07^{+0.03}_{-0.03}$	$1.61^{+0.2}_{-0.18}$	$-1.43^{+0.05}_{-0.05}$	$0.41^{+0.09}_{-0.09}$
IC 5332	$5.33^{+0.48}_{-0.44}$	$-0.59^{+0.03}_{-0.03}$	$-0.4^{+0.14}_{-0.14}$	$5.33^{+0.48}_{-0.44}$	$-0.59^{+0.03}_{-0.03}$	$0.09^{+0.04}_{-0.04}$
KK 197	$4.99^{+0.51}_{-0.46}$	$-2.16^{+0.06}_{-0.06}$	…	$4.85^{+0.93}_{-0.78}$	$-1.32^{+0.11}_{-0.11}$	…
KK S58	$0.64^{+0.11}_{-0.09}$	$-1.87^{+0.09}_{-0.09}$	$0.14^{+0.02}_{-0.02}$	$0.14^{+0.04}_{-0.03}$	$-1.84^{+0.2}_{-0.2}$	$-0.07^{+0.02}_{-0.02}$
NGC 1487	$1.91^{+0.34}_{-0.29}$	$-1.2^{+0.12}_{-0.12}$	$-0.17^{+0.28}_{-0.28}$	$0.97^{+0.11}_{-0.1}$	$-0.59^{+0.05}_{-0.05}$	$0.85^{+0.03}_{-0.03}$
NGC 1705	$12.56^{+0.6}_{-0.57}$	$-1.66^{+0.07}_{-0.07}$	$-0.03^{+0.04}_{-0.04}$	$0.21^{+0.02}_{-0.02}$	$-1.53^{+0.06}_{-0.06}$	$-0.32^{+0.11}_{-0.11}$
NGC 1796	$0.29^{+0.12}_{-0.09}$	$-0.62^{+0.19}_{-0.19}$	$0.72^{+0.01}_{-0.01}$	$12.74^{+0.62}_{-0.59}$	$-1.32^{+0.04}_{-0.04}$	$0.23^{+0.0}_{-0.0}$
NGC 2835	$1.36^{+0.14}_{-0.13}$	$-0.49^{+0.03}_{-0.03}$	$0.39^{+0.06}_{-0.06}$	$1.15^{+0.1}_{-0.09}$	$-0.18^{+0.03}_{-0.03}$	$0.11^{+0.03}_{-0.03}$
NGC 3274	$1.2^{+0.15}_{-0.13}$	$-2.0^{+0.06}_{-0.06}$	$-0.07^{+0.05}_{-0.05}$	$2.1^{+0.37}_{-0.31}$	$-1.24^{+0.08}_{-0.08}$	$0.88^{+0.03}_{-0.03}$
NGC 3368	$1.53^{+0.09}_{-0.08}$	$0.23^{+0.04}_{-0.04}$	$0.0^{+0.04}_{-0.04}$	$5.03^{+0.38}_{-0.35}$	$-0.18^{+0.04}_{-0.04}$	$0.13^{+0.01}_{-0.01}$
NGC 3489	$3.15^{+0.39}_{-0.35}$	$0.15^{+0.08}_{-0.08}$	$0.14^{+0.03}_{-0.03}$	$3.1^{+0.22}_{-0.2}$	$-0.23^{+0.04}_{-0.04}$	$0.12^{+0.09}_{-0.09}$
NGC 3593	$5.33^{+0.8}_{-0.7}$	$-0.28^{+0.15}_{-0.15}$	$0.11^{+0.02}_{-0.02}$	$12.07^{+0.86}_{-0.8}$	$-0.49^{+0.03}_{-0.03}$	$0.13^{+0.11}_{-0.11}$
NGC 4592	$0.13^{+0.02}_{-0.02}$	$-0.22^{+0.07}_{-0.07}$	$-0.02^{+0.08}_{-0.08}$	$0.49^{+0.04}_{-0.04}$	$-0.61^{+0.02}_{-0.02}$	$0.11^{+0.06}_{-0.06}$
NGC 5253	$0.21^{+0.05}_{-0.04}$	$-1.47^{+0.12}_{-0.12}$	…	$0.54^{+0.1}_{-0.09}$	$-1.67^{+0.1}_{-0.1}$	…
NGC 853	$4.07^{+0.41}_{-0.38}$	$-1.42^{+0.05}_{-0.05}$	$-0.0^{+0.0}_{-0.0}$	$3.13^{+0.39}_{-0.34}$	$-1.6^{+0.06}_{-0.06}$	$0.36^{+0.06}_{-0.06}$
UGC 3755	$0.09^{+0.02}_{-0.02}$	$-1.64^{+0.3}_{-0.3}$	…	$1.82^{+0.24}_{-0.21}$	$-1.37^{+0.12}_{-0.12}$	…
UGC 5889	$5.88^{+0.68}_{-0.61}$	$-1.28^{+0.05}_{-0.05}$	$0.45^{+0.07}_{-0.07}$	$1.02^{+0.19}_{-0.16}$	$-0.51^{+0.05}_{-0.05}$	$-0.01^{+0.02}_{-0.02}$
UGC 8041	$0.35^{+0.05}_{-0.04}$	$-0.51^{+0.07}_{-0.07}$	$-0.12^{+0.0}_{-0.0}$	$3.34^{+0.39}_{-0.35}$	$-0.47^{+0.05}_{-0.05}$	$0.48^{+0.27}_{-0.27}$

ORCID iDs

Hong-Xin Zhang https://orcid.org/0000-0003-1632-2541
Sanjaya Paudel https://orcid.org/0000-0002-8040-6902
Yimeng Tang https://orcid.org/0000-0003-2876-577X
Guangwen Chen https://orcid.org/0000-0002-4742-8800
Xu Kong https://orcid.org/0000-0002-7660-2273

References

Ahn, C. P., Seth, A. C., den Brok, M., et al. 2017, ApJ, 839, 72
Alfaro-Cuello, M., Kacharov, N., Neumayer, N., et al. 2020, ApJ, 892, 20
Antonini, F., Barausse, E., & Silk, J. 2015, ApJ, 812, 72
Arca-Sedda, M., & Capuzzo-Dolcetta, R. 2014, MNRAS, 444, 3738
Atallah, D., Trani, A. A., Kremer, K., et al. 2023, MNRAS, 523, 4227
Bacon, R., Conseil, S., Mary, D., et al. 2017, A&A, 608, A1
Barbary, K. 2016, extinction v0.3.0, Zenodo, doi:10.5281/zenodo.804967
Bekki, K. 2010, MNRAS, 401, 2753
Bekki, K. 2015, ApJL, 812, L14
Binney, J., & Tremaine, S. 1987, Galactic Dynamics (Princeton, NJ: Princeton Univ. Press)
Calzetti, D., Johnson, K. E., Adamo, A., et al. 2015, ApJ, 811, 75
Cappellari, M. 2017, MNRAS, 466, 798
Cappellari, M., & Emsellem, E. 2004, PASP, 116, 138
Capuzzo-Dolcetta, R. 1993, ApJ, 415, 616
Cardelli, J. A., Clayton, G. C., & Mathis, J. S. 1989, ApJ, 345, 245
Carlsten, S. G., Greene, J. E., Beaton, R. L., & Greco, J. P. 2022, ApJ, 927, 44
Chen, G., Zhang, H.-X., Kong, X., et al. 2022, ApJL, 934, L35
Consolandi, G., Gavazzi, G., Fumagalli, M., Dotti, M., & Fossati, M. 2016, A&A, 591, A38
Côté, P., Piatek, S., Ferrarese, L., et al. 2006, ApJS, 165, 57
Davidson, R., & Flachaire, E. 2008, J. Econometrics, 146, 162
de Vaucouleurs, G., de Vaucouleurs, A., Corwin, H. G., Jr., et al. 1991, Third Reference Catalogue of Bright Galaxies (New York: Springer)

den Brok, M., Peletier, R. F., Seth, A., et al. 2014, MNRAS, 445, 2385
Fahrion, K., Bulichi, T.-E., Hilker, M., et al. 2022b, A&A, 667, A101
Fahrion, K., Leaman, R., Lyubenova, M., & van de Ven, G. 2022a, A&A, 658, A172
Fahrion, K., Lyubenova, M., van de Ven, G., et al. 2021, A&A, 650, A137
Fahrion, K., Müller, O., Rejkuba, M., et al. 2020, A&A, 634, A53
Feldmeier-Krause, A., Neumayer, N., Schödel, R., et al. 2015, A&A, 584, A2
Fouesneau, M. 2022, pyphot, v1.4.3, Zenodo, doi:10.5281/zenodo.7016775
Fragione, G., & Silk, J. 2020, MNRAS, 498, 4591
Georgiev, I. Y., Böker, T., Leigh, N., Lützgendorf, N., & Neumayer, N. 2016, MNRAS, 457, 2122
Graham, A. W., Merritt, D., Moore, B., Diemand, J., & Terzić, B. 2006, AJ, 132, 2711
Graham, A. W., & Spitler, L. R. 2009, MNRAS, 397, 2148
Guillard, N., Emsellem, E., & Renaud, F. 2016, MNRAS, 461, 3620
Harris, W. E., Blakeslee, J. P., & Harris, G. L. H. 2017, ApJ, 836, 67
Hoyer, N., Neumayer, N., Georgiev, I. Y., Seth, A. C., & Greene, J. E. 2021, MNRAS, 507, 3246
Hoyer, N., Neumayer, N., Seth, A. C., Georgiev, I. Y., & Greene, J. E. 2023a, MNRAS, 520, 4664
Hoyer, N., Pinna, F., Kamlah, A. W. H., et al. 2023b, ApJL, 944, L25
Johnston, E. J., Puzia, T. H., D'Ago, G., et al. 2020, MNRAS, 495, 2247
Jordán, A., McLaughlin, D. E., Côté, P., et al. 2007, ApJS, 171, 101
Kacharov, N., Neumayer, N., Seth, A. C., et al. 2018, MNRAS, 480, 1973
Karachentsev, I. D., Makarov, D. I., & Kaisina, E. I. 2013, AJ, 145, 101
Knowles, A. T., Sansom, A. E., Vazdekis, A., & Allende Prieto, C. 2023, MNRAS, 523, 3450
Kourkchi, E., & Tully, R. B. 2017, ApJ, 843, 16
Leaman, R., & van de Ven, G. 2022, MNRAS, 516, 4691
Lim, S., Peng, E. W., Côté, P., et al. 2024, ApJ, 966, 168
Liu, C., Côté, P., Peng, E. W., et al. 2020, ApJS, 250, 17
Liu, C., Peng, E. W., Côté, P., et al. 2015, ApJ, 812, 34
Lotz, J. M., Telford, R., Ferguson, H. C., et al. 2001, ApJ, 552, 572
Mayes, R. J., Drinkwater, M. J., Pfeffer, J., et al. 2021, MNRAS, 501, 1852
Mihos, J. C., & Hernquist, L. 1994, ApJL, 437, L47
Miller, M. C., & Lauburg, V. M. 2009, ApJ, 692, 917
Mowla, L., van der Wel, A., van Dokkum, P., & Miller, T. B. 2019, ApJL, 872, L13
Neumayer, N., Seth, A., & Böker, T. 2020, A&ARv, 28, 4
Neumayer, N., & Walcher, C. J. 2012, AdAst, 2012, 709038
Nguyen, D. D., Bureau, M., Thater, S., et al. 2022, MNRAS, 509, 2920
Nguyen, D. D., Seth, A. C., Neumayer, N., et al. 2018, ApJ, 858, 118
Paudel, S., Lisker, T., & Kuntschner, H. 2011, MNRAS, 413, 1764
Paudel, S., Lisker, T., Kuntschner, H., Grebel, E. K., & Glatt, K. 2010, MNRAS, 405, 800
Paudel, S., & Yoon, S.-J. 2020, ApJL, 898, L47
Pechetti, R., Seth, A., Neumayer, N., et al. 2020, ApJ, 900, 32
Peng, E. W., Jordán, A., Côté, P., et al. 2006, ApJ, 639, 95
Relatores, N. C., Newman, A. B., Simon, J. D., et al. 2019, ApJ, 887, 94
Rhee, J., Smith, R., Choi, H., et al. 2017, ApJ, 843, 128
Rodríguez-Puebla, A., Primack, J. R., Avila-Reese, V., & Faber, S. M. 2017, MNRAS, 470, 651
Román, J., Sánchez-Alarcón, P. M., Knapen, J. H., & Peletier, R. 2023, A&A, 671, L7
Rossa, J., van der Marel, R. P., Böker, T., et al. 2006, AJ, 132, 1074
Sánchez-Janssen, R., Côté, P., Ferrarese, L., et al. 2019, ApJ, 878, 18
Schiavi, R., Capuzzo-Dolcetta, R., Georgiev, I. Y., Arca-Sedda, M., & Mastrobuono-Battisti, A. 2021, MNRAS, 503, 594
Schlegel, D. J., Finkbeiner, D. P., & Davis, M. 1998, ApJ, 500, 525
Seth, A. C., Dalcanton, J. J., Hodge, P. W., & Debattista, V. P. 2006, AJ, 132, 2539
Silk, J., Wyse, R. F. G., & Shields, G. A. 1987, ApJL, 322, L59
Smith, R., Pacifici, C., Pasquali, A., & Calderón-Castillo, P. 2019, ApJ, 876, 145
Spengler, C., Côté, P., Roediger, J., et al. 2017, ApJ, 849, 55
Tang, Y., Tao, B., Zhang, H.-X., et al. 2022, A&A, 668, A179
Thomas, D., Maraston, C., & Bender, R. 2003, MNRAS, 339, 897
Tremaine, S. D., Ostriker, J. P., & Spitzer, L., Jr. 1975, ApJ, 196, 407
Turner, M. L., Côté, P., Ferrarese, L., et al. 2012, ApJS, 203, 5
Vazdekis, A., Sánchez-Blázquez, P., Falcón-Barroso, J., et al. 2010, MNRAS, 404, 1639
Vernet, J., Dekker, H., D'Odorico, S., et al. 2011, A&A, 536, A105
Walcher, C. J., Böker, T., Charlot, S., et al. 2006, ApJ, 649, 692
Wang, K., Peng, E. W., Liu, C., et al. 2023, Natur, 623, 296
Zhang, H.-X., Peng, E. W., Côté, P., et al. 2015, ApJ, 802, 30
Zhang, H.-X., Puzia, T. H., Peng, E. W., et al. 2018, ApJ, 858, 37
Zinn, R., & West, M. J. 1984, ApJS, 55, 45